
GRADO EN INGENIERÍA EN TECNOLOGÍAS INDUSTRIALES

TRABAJO FIN DE GRADO

# Progressive Failure Analysis of FFF Additively Manufactured Parts

Author: Mª Cristina Garicano Nuez

Director: Mehran Tehrani

Madrid 2020

COMILLAS
UNIVERSIDAD PONTIFICIA
ICAI

GRADO EN INGENIERÍA EN TECNOLOGÍAS INDUSTRIALES

TRABAJO FIN DE GRADO

# Progressive Failure Analysis of FFF Additively Manufactured Parts

Autor: Mª Cristina Garicano Nuez

Director: Mehran Tehrani

Madrid 2020

# ANÁLISIS DEL FALLO PROGRESIVO DE PIEZAS FABRICADAS MEDIANTE FABRICACIÓN POR ADICIÓN

**Autor: Garicano Nuez, Mª Cristina**

Director: Tehrani, Mehran

Entidad Colaboradora: University of Texas at Austin

## RESUMEN DEL PROYECTO

En el ámbito de este trabajo, la teoría clásica de laminación (CLT) se utilizó para modelar las piezas fabricadas a través de la fabricación de filamentos fundidos (FFF). Los resultados evidencian que no se consigue mayor resistencia en las piezas optimizando el ángulo de trama y el fallo de las piezas no será progresivo en la mayoría de los casos. Además, se caracterizó una superficie de fallo utilizando un criterio basado en un tensor de resistencia con interacción de esfuerzos.

**Palabras clave**: Fabricación por Filamentos Fundidos, fallo progresivo, superficie de fallo.

### 1. Introducción

La fabricación aditiva (AM) es una técnica prometedora tanto para la creación rápida de prototipos como para la fabricación de piezas funcionales. Las piezas se forman capa por capa a partir de un modelo tridimensional de diseño asistido por ordenador (CAD). Las principales ventajas de la AM implican la creación de formas complejas, que de otro modo serían imposibles para las técnicas de fabricación tradicionales, sin necesidad de herramientas o moldes caros [1, 2]. También reduce el coste y el tiempo de ciclo del desarrollo del producto y permite el uso de múltiples materiales en la misma pieza [3, 4]. Las tecnologías AM son particularmente adecuadas para la impresión de sistemas totalmente funcionales, la personalización masiva, la fabricación descentralizada y la fabricación bajo demanda. Algunas aplicaciones incluyen la salud, la automoción, la industria aeroespacial y la electrónica [1, 3-5].

La fabricación de filamentos fundidos (FFF) es la técnica más madura, popular y de más rápido crecimiento [6]. Un filamento fundido de un material termoplástico se extruye y se deposita sobre la cama de impresión para formar la geometría final. La adición de un

material de refuerzo, como la fibra de carbono, puede mejorar las propiedades mecánicas y la estabilidad térmica de los polímeros utilizados para la impresión [1].

## 2. Definición del proyecto

Las piezas impresas mediante FFF serán estudiadas con los siguientes objetivos:

- Comparación del fallo de la primera capa (FPF) con respecto al fallo de la última (LPF). Esto determinará cuándo se puede observar un fallo progresivo.
- Optimización del ángulo de trama para conseguir piezas más resistentes sometidas cargas biaxiales.
- Implementación del alcance del límite elástico en la segunda dirección.
- Caracterización de una superficie de fallo.

## 3. Definición del modelo

### 3.1. Análisis CLT

Las piezas impresas mediante FFF pueden ser tratadas como compuestos laminados y modeladas con la teoría clásica de laminación (CLT). En este trabajo se estudian diferentes secuencias de apilamiento bajo cargas mecánicas representativas para predecir su rendimiento.

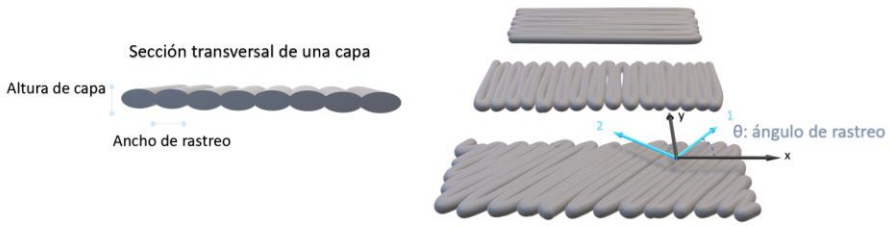


*Figura 1: Parámetros de procesamiento*

Como resultado de la impresión FFF, las piezas tienen propiedades anisótropas. La resistencia en la dirección de los filamentos es mayor que en la dirección transversal. Las propiedades mecánicas dependen de los parámetros de procesamiento: el espesor de la capa, el ancho de la trama, el ángulo de la trama o la temperatura de impresión, por ejemplo. Estos parámetros se ilustran en la Figura 1: Parámetros de procesamientoFigura 1.

En el ámbito de este trabajo, se estudiará el comportamiento de las piezas bajo diferentes cargas. Se utilizarán dos criterios de forma comparativa para establecer el fallo de la pieza. Uno más conservador que considera el fallo cuando la primera capa se rompe. Las capas más débiles se van descontando hasta que solo quede una; el segundo criterio considera el fallo de esta última capa. Bajo cargas biaxiales, en los materiales compuestos, alineando las fibras con la dirección principal de la carga se consiguen las mejores piezas. Se optimizará el ángulo de trama con la intención de conseguir resultados similares.

### 3.2. Superficie de fallo

El criterio de fallo propuesto fue desarrollado por Osswald y Osswald [7]. Se basa en el método descrito por Gol'denblat y Kopnov [8] y se ha mejorado para superar algunas de sus limitaciones.

El criterio original describe la siguiente función escalar que depende de los tensores de fuerza y el estado de tensión:

$$f = \left(F_{ij}\sigma_{ij}\right)^{\alpha} + \left(F_{ijkl}\sigma_{ij}\sigma_{kl}\right)^{\beta} + \left(F_{ijklmn}\sigma_{ij}\sigma_{kl}\sigma_{mn}\right)^{\gamma} \ldots$$

A los parámetros α y β se les asignaron los valores de 1 y 1/2 respectivamente para mantener una relación escalar lineal con las tensiones. El fallo ocurrirá para los estados de tensión con un valor de *f* mayor que 1. Para un escenario de tensión plano, el criterio se reduce a:

$$f = F_{11}\sigma_{11} + F_{22}\sigma_{22} + F_{12}\tau_{12} + \left(F_{1111}\sigma_{11}^2 + F_{2222}\sigma_{22}^2 + F_{1212}\tau_{12}^2 + 2F_{1122}\sigma_{11}\sigma_{22} + 2F_{1112}\sigma_{11}\tau_{12} + 2F_{2212}\sigma_{22}\tau_{12}\right)^{\frac{1}{2}}$$

Donde la notación $\sigma_{ij}$ y $\tau_{ij}$ indican tensiones axiales y de cortantes, y los términos $F_{ij}$, $F_{ijkl}$ representan los tensores de segundo y cuarto orden que dependen de los parámetros de resistencia del material.

La novedad de este criterio es la aplicación de la interacción entre los esfuerzos axiales y de cortantes. Realizando pruebas mecánicas en lugares estratégicos, se puede conocer la pendiente de la superficie de fallo.

# 4. Resultados

## 4.1. Análisis CLT

La secuencia de apilamiento [0, ±θ]s fue estudiada bajo una carga uniaxial en la dirección *x*. Los resultados y un esquema de la secuencia de apilamiento se muestran en la Figura 2.

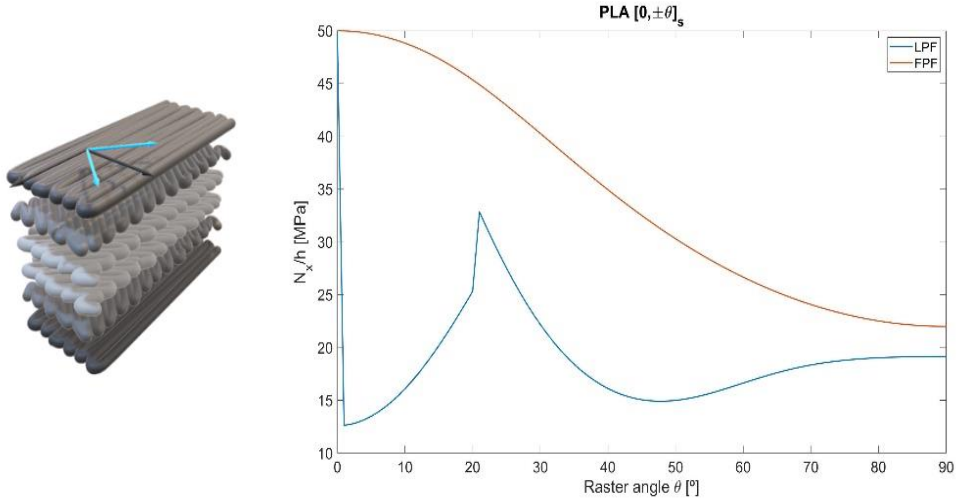


*Figura 2: Secuencia de procesamiento[0,±θ]s. PLA máxima carga entre la altura frente a el ángulo de trama.*

La pieza más resistente se logra cuando todos los filamentos están alineados con la carga. En cuanto el ángulo de la trama aumenta, el fallo de la última capa disminuye notablemente. En el análisis CLT, la carga se distribuye dependiendo de la rigidez de cada capa. En el caso de estas piezas, como el módulo elástico es isotrópico, las tensiones son las mismas en todas las capas. Po eso, una vez que se descuentan las capas más débiles, las capas restantes por sí solas no pueden soportar la carga. De esta forma, el fallo observado será repentino, no será progresivo. Si se añaden otras dos capas alineadas con la carga, entonces la línea del fallo de la última capa se desplaza verticalmente hacia arriba, y se observará un fallo progresivo para valores altos del ángulo de trama. Para el material estudiado, PLA, debe haber al menos el mismo número de capas alineadas con la carga que el número de capas con una orientación diferente.

Para optimizar el ángulo rasterizado bajo una carga combinada, una pieza con la secuencia [±θ]s fue sometida a una carga biaxial. La relación entre la carga en la

dirección *x* y la dirección *y* fue 5. La Figura 3 muestra un esquema de la secuencia de apilamiento y los resultados.

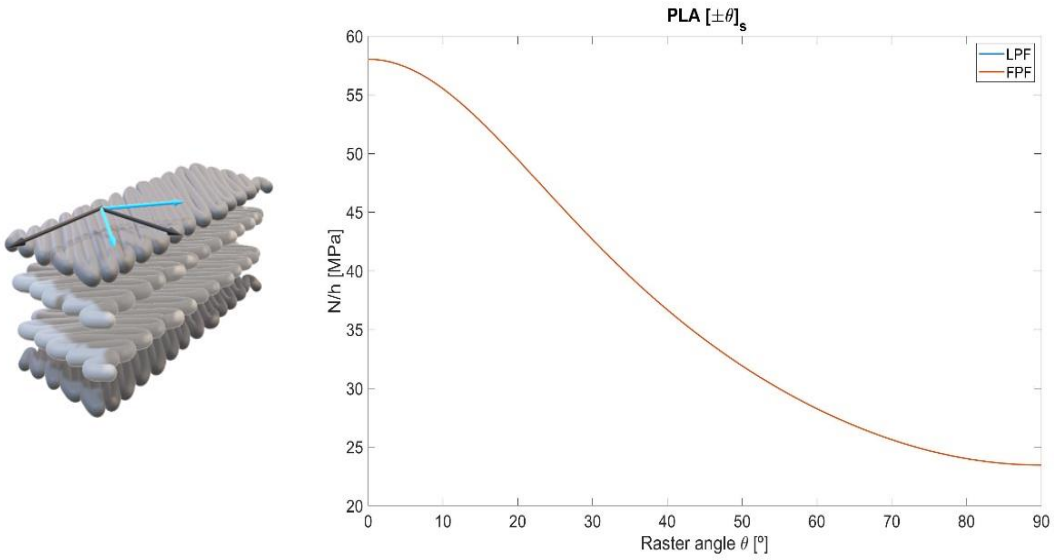


*Figura 3: : Secuencia de trama [±θ]s. PLA máxima carga entre la altura frente al ángulo de rasterizado.*

La carga más alta puede ser soportada por las partes con todos los filamentos alineados con el componente más alto de la fuerza externa. En este caso el máximo local no se alcanza para las partes con las fibras alineadas con la dirección principal de la carga, como es el caso de los composites. La resistencia de la primera y la segunda dirección son de la misma magnitud, por lo que las capas son capaces de sostener la carga de la dirección transversal sin romperse. Además, la interacción entre las tensiones tiene un efecto de refuerzo y, por lo tanto, la carga máxima que soportan es incluso mayor que en el caso de la carga uniaxial.

Por último, se consideró el efecto del alcance del límite elástico en la segunda dirección, pero el impacto en el comportamiento de las piezas fue insignificante.

### 4.2. Superficie de fallo

La función de fallo se caracterizó para el material nylon PA6 reforzado con fibra de carbono.

La interacción entre las tensiones se captura con el parámetro $F_{1122}$ como se muestra en la Figura 4. Este valor está limitado por la condición de estabilidad y debe tomar un valor entre:

$$-\sqrt{F_{1111}F_{2222}} \leq F_{1122} \leq \sqrt{F_{1111}F_{2222}}$$

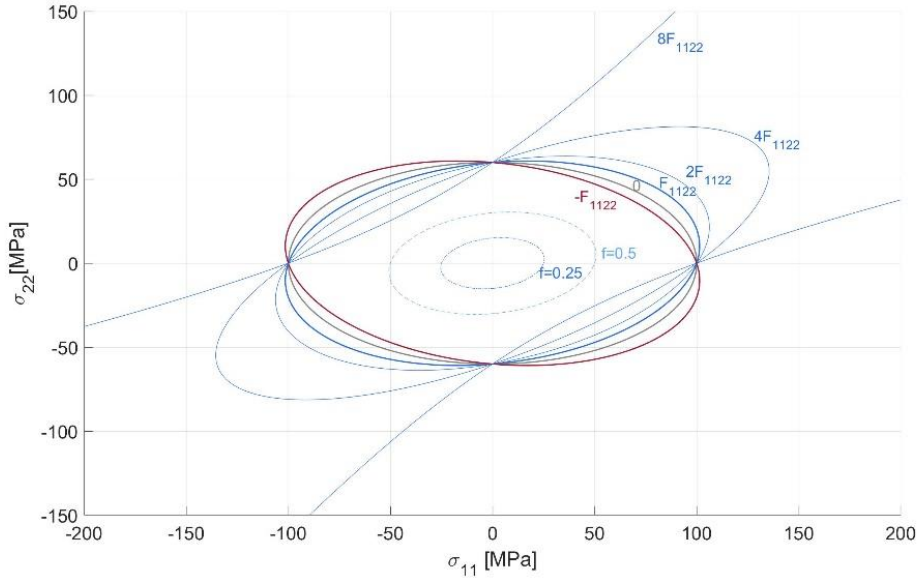


*Figura 4: Función de fallo en el plano σ11-σ22*

Si el valor de $F_{1122}$ está fuera del rango, la función no describirá una superficie cerrada, lo que significa que hay algunos estados de tensión en los que la pieza nunca fallaría.

Para capturar la interacción entre el esfuerzo cortante y las tensiones, la pendiente ($\mu_{ii12}$) de la superficie de fallo puede ajustarse a los datos experimentales en un plano de esfuerzos cortante-axial. Una pendiente positiva refleja una interacción de refuerzo entre el cortante y tensiones positivas, como puede observarse en la Figura 5.

Por último, la superficie de fallo se representa en el espacio σ11-σ22-τ12 en la Figura 6. Los factores de seguridad de 1, ¾, 2 y 4 están representados por *f*=1, 0.75, 0.5 y 0.25, respectivamente.

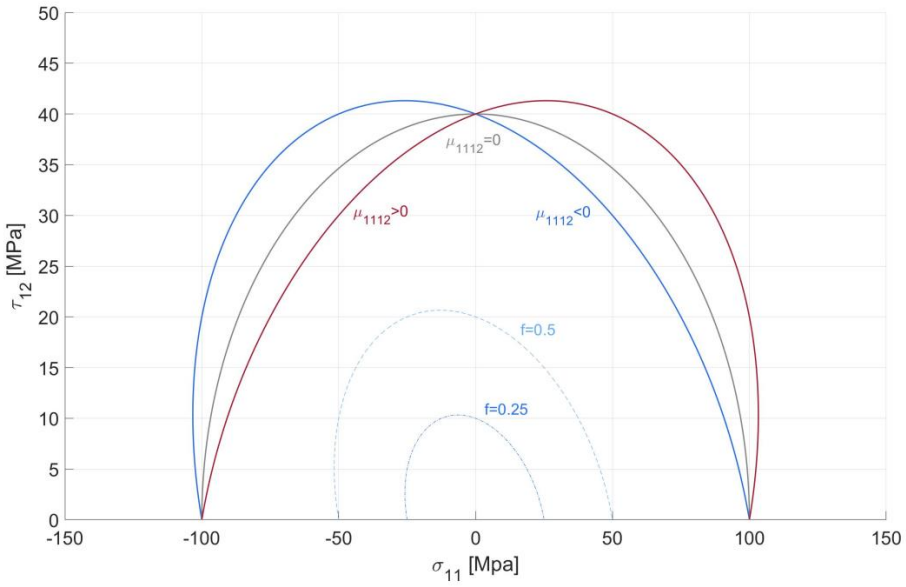


*Figura 5: Superficie de fallo en el plano axial-cortante σ11-τ12*

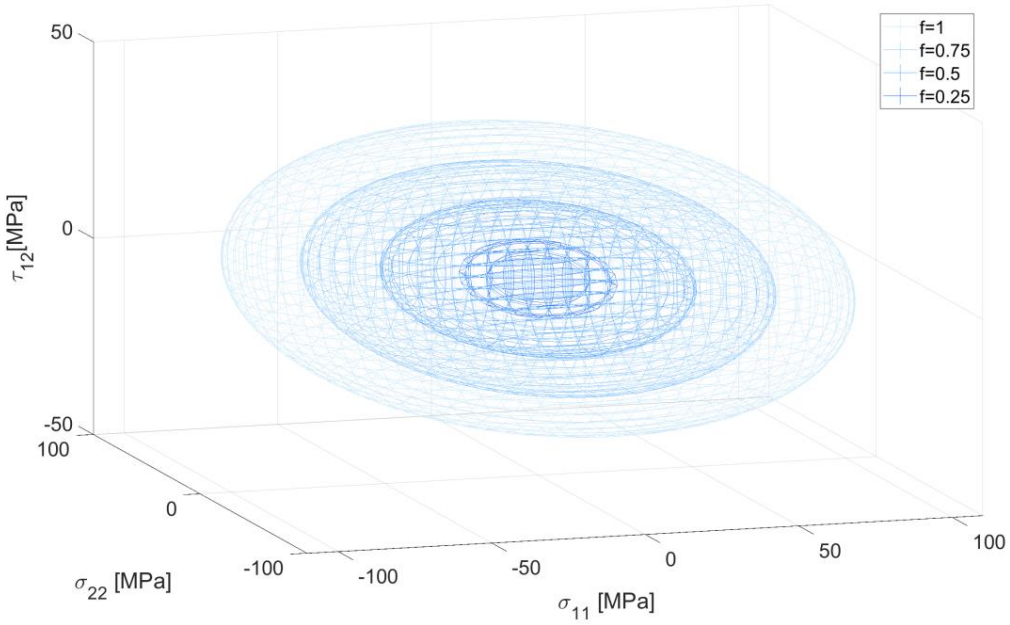


*Figura 6: Superficie de fallo en 3D para CF nylon*

## 5. Conclusiones

El fallo progresivo no se observa en las piezas impresas de FFF como en los materiales compuestos. El grado de anisotropía en su resistencia no es suficiente para que las capas sostengan la carga cuando las capas más débiles fallan en muchas secuencias de apilamiento. En el caso del PLA debe haber al menos el mismo número de capas

alineadas con la carga que el número con un ángulo de trama diferente. Incluso en esos casos, el fallo progresivo sólo se observa para valores altos del ángulo rasterizado, cuando las capas más débiles fallan de forma transversal.

Las mejores piezas se lograrán alineando las fibras con el componente más alto de la carga externa. En un caso biaxial, cuando ambos componentes tienen el mismo signo, si la dirección transversal no falla, la interacción entre las tensiones reforzará la resistencia de las piezas.

El criterio de fallo desarrollado por Osswald y Osswald [7] es capaz de caracterizar el fallo de las piezas captando las interacciones entre todos los esfuerzos. Con pruebas experimentales, puede ser implementado en un software de simulación para determinar una región de seguridad para los estados de tensión.

## 6. Referencias


1. Goncalves, J., et al., *Electrically Conductive Polyetheretherketone Nanocomposite Filaments: From Production to Fused Deposition Modeling.* Polymers (Basel), 2018. **10**(8).
2. Rinaldi, M., et al., *Additive layer manufacturing of poly (ether ether ketone) via FDM.* Composites Part B: Engineering, 2018. **145**: p. 162-172.
3. Gebisa, A.W., *Influence of 3D Printing FDM Proce.* 2019.
4. Wu, W., et al., *Influence of Layer Thickness and Raster Angle on the Mechanical Properties of 3D-Printed PEEK and a Comparative Mechanical Study between PEEK and ABS.* Materials (Basel), 2015. **8**(9): p. 5834-5846.
5. Wang, P., et al., *Effects of printing parameters of fused deposition modeling on mechanical properties, surface quality, and microstructure of PEEK.* Journal of Materials Processing Technology, 2019. **271**: p. 62-74.
6. Gebisa, A.W. and H.G. Lemu, *Investigating Effects of Fused-Deposition Modeling (FDM) Processing Parameters on Flexural Properties of ULTEM 9085 using Designed Experiment.* Materials (Basel), 2018. **11**(4).
7. Osswald, P.V. and T.A. Osswald, *A strength tensor based failure criterion with stress interactions.* Polymer Composites, 2018. **39**(8): p. 2826-2834.
8. Gol'denblat, I.I. and V.A. Kopnov, *Strength of glass-reinforced plastics in the complex stress state.* Polymer Mechanics, 1965. **1**(2): p. 54-59.

# PROGRESSIVE FAILURE ANALYSIS OF FFF ADDITIVELY MANUFACTURED PARTS

**Author: Garicano Nuez, Mª Cristina.**

Supervisor: Tehrani, Mehran.

Collaborating Entity: University of Texas at Austin.

## ABSTRACT

In the scope of this work, the classical lamination theory (CLT) was used to model parts manufactured via Fused Filament Fabrication (FFF). The results evidence that parts are likely to experience sudden failure and there is no improvement in the strength by optimizing the raster angle. In addition, a failure surface for FFF parts was characterized using a strength tensor-based criterion with stress interaction.

**Key words**: Fused Filament Fabrication, progressive failure, failure criterion.

## 1. Introduction

Additive manufacturing (AM) is a promising technique for both rapid prototyping and fabricating functional parts. Parts are formed layer by layer from a three-dimensional computer aided design (CAD) model. The main advantages of AM involve the creation of complex shapes, which would otherwise be impossible for traditional manufacturing techniques, without the need of expensive tooling or molds[1, 2]. It also reduces the cost and the cycle time of product development and enables the use of multiple materials in the same part [3, 4]. AM technologies are particularly suitable for printing fully functional systems, mass customization, decentralized and on-demand manufacturing. Some applications include healthcare, automotive, aerospace and electronics [1, 3-5].

Fused Filament Fabrication (FFF) is the most mature, popular, and fastest growing of all the techniques [6]. A melted filament of a thermoplastic material is extruded and deposited on a heated bed to form the final geometry. The addition of a reinforcement material, like carbon fiber, can improve the mechanical properties and thermal stability of the printed polymers [1].

## 2. Project definition

FFF printed parts will be studied with the following objectives:

- Comparison of the first ply failure versus the last ply failure. This will determine when progressive failure can be observed.
- Optimization of the raster angle to achieve stronger parts under biaxial loads.
- Implementation of the effect of yielding in the second direction in the laminate behavior.
- Characterization of a failure surface.

## 3. Model description

### 3.1. CLT Analysis

FFF printed parts can be treated as laminated composites and modeled with the classical lamination theory (CLT). Different stacking sequences are studied under representative mechanical loads to predict their performance.

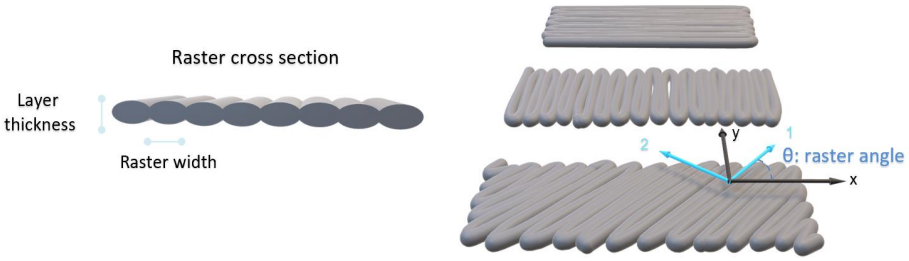


*Figure_ 1: Processing parameters*

As a result of FFF printing, the parts have anisotropic properties. The strength in the direction of the filaments is higher than in the transverse direction. The mechanical properties are dependent on the processing parameters: layer thickness, raster width, raster angle or printing temperature for instance. These parameters are illustrated in Figure_ 1.

The first ply failure occurs when the first ply breaks. Once the weaker layers fail, they are progressively discounted until there is only one last ply. When the last ply breaks, the failure is considered for the last ply failure.

In the scope of this work, the behavior of parts under biaxial loads will be studied. In composite materials aligning the fibers with the principal direction of the load achieves the best parts.

### 3.2. Failure surface

The failure criterion proposed was developed by Osswald and Osswald [7]. It is based on the method described by Gol'denblat and Kopnov [8] and improved to overcome some of its limitations.

The original criterion describes the following scalar function that depends on the strength tensors and the stress state:

$$f = \left(F_{ij}\sigma_{ij}\right)^{\alpha} + \left(F_{ijkl}\sigma_{ij}\sigma_{kl}\right)^{\beta} + \left(F_{ijklmn}\sigma_{ij}\sigma_{kl}\sigma_{mn}\right)^{\gamma} \ldots$$

The parameters α and β were assigned the values of 1 and $\frac{1}{2}$ respectively in order to maintain a linear scalar relationship with the stresses. Failure is expected for stress states with a value of *f* greater than 1. For a plane stress scenario, the criterion is reduced to:

$$f = F_{11}\sigma_{11} + F_{22}\sigma_{22} + F_{12}\tau_{12} + (F_{1111}\sigma_{11}^2 + F_{2222}\sigma_{22}^2 + F_{1212}\tau_{12}^2 + 2F_{1122}\sigma_{11}\sigma_{22} + 2F_{1112}\sigma_{11}\tau_{12} + 2F_{2212}\sigma_{22}\tau_{12})^{\frac{1}{2}}$$

Where the notation $\sigma_{ij}$ and $\tau_{ij}$ indicate axial and shear stresses, and the terms $F_{ij}$, $F_{ijkl}$ represent the second and fourth order tensors that depend on engineering strength parameters.

The novelty of this criterion is the implementation of the interaction between the axial and shear stresses. By performing mechanical tests in strategic locations, the slope of the failure surface can be known.

## 4. Results

### 4.1. CLT Analysis

The stacking sequence $[0,\pm\theta]_s$ was studied under a uniaxial load in the x direction. The results and a schematic of the stacking sequence are shown in Figure_ 2.

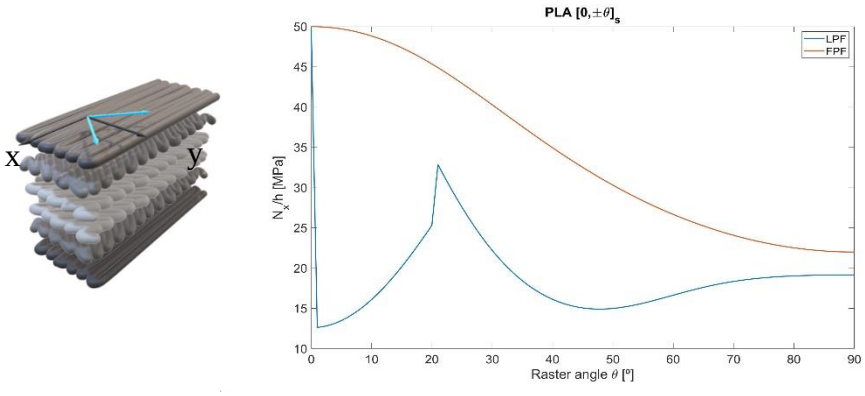


*Figure_ 2: Stacking sequence [0,±θ]s. PLA maximum load over height versus raster angle*

The strongest part is achieved when all the filaments are aligned with the load. As the raster angle increases, the last ply failure drops. In the CLT analysis, the load is distributed depending on the stiffness of each ply. Since the elastic modulus is isotropic, the stresses are the same in all the layers. Once the weaker plies are discounted, the remaining layers alone cannot hold the load. Therefore the failure will be sudden, no progressive failure is observed. If another two layers aligned with the load are added, then the last ply failure line is shifted, and progressive failure will be observed for high values of the raster angle. There must be at least the same number of layers aligned with the load as the number of layers with a different orientation.

To optimize the raster angle under a combined load, a $[\pm\theta]_s$ laminate was subject to a biaxial load. The ratio between the load in the *x* direction and *y* direction was 5. Figure_ 3**Error! Reference source not found.** shows a schematic of the stacking sequence and the results.

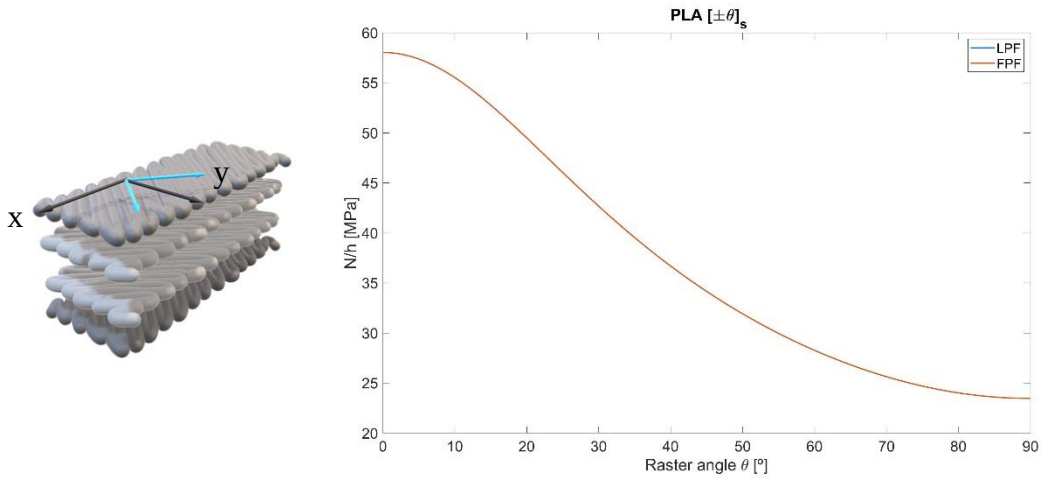


*Figure_ 3: Stacking sequence [±θ]s. PLA maximum load over height versus raster angle*

The highest load can be supported by the parts with all the filaments aligned with the highest component of the external force. In this case the local maximum is not achieved for parts with the fibers aligned with the principal direction of the load, as it was the case for composites. The strengths in the first and second direction are of the same magnitude, so the layers are able to hold the load in the transverse direction without failure. Moreover, the interaction between the stresses has a strengthening effect and thus the load is even higher than in the uniaxial load case.

Lastly, the effect of yielding in the second direction was considered but the impact on the laminate behavior was negligible.

### 4.2. Failure surface

The failure function was characterized for carbon fiber nylon PA6 material.

The interaction between the stresses is captured with the parameter $F_{1122}$ as shown in Figure_ 4**Error! Reference source not found.**. The value of $F_{1122}$ is bounded by the stability condition and must take a value between:

$$-\sqrt{F_{1111}F_{2222}} \leq F_{1122} \leq \sqrt{F_{1111}F_{2222}}$$

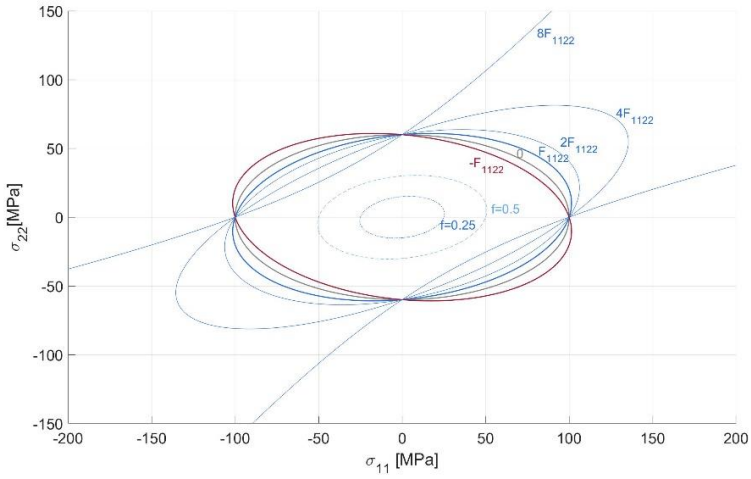


*Figure_ 4: Failure envelope in the axial stress plane σ11-σ22*

If the value of $F_{1122}$ is outside the range, the function would not describe a closed surface, meaning there are some stress states where the part would never fail.

To capture the interaction between shear and the stresses, the slope ($\mu_{ii12}$) of the failure surface can be fitted to experimental data in an axial-shear plane. A positive slope reflects a strengthening interaction between the shear and positive stresses as it can be observed in Figure_ 5.

Finally, the failure surface is plotted in the $\sigma_{11}$-$\sigma_{22}$-$\tau_{12}$ space in Figure_ 6. The safety factors of 1, ¾, 2 and 4 are represented by *f*=1, 0.75, 0.5 and 0.25 ,respectively.

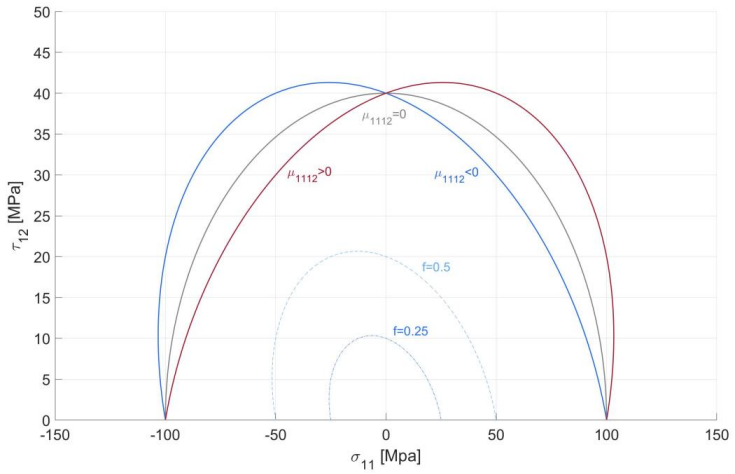


*Figure_ 5: Failure envelope in the shear axial stress plane σ11-τ12*

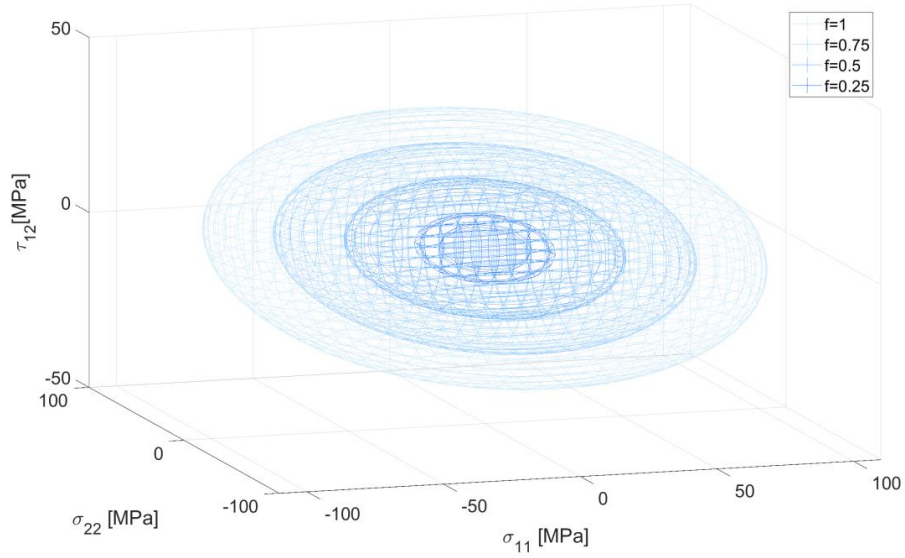


*Figure_ 6: 3D failure surface for CF nylon*

## 5. Conclusions

Progressive failure is not observed for FFF printed parts as it is for composites. The degree of anisotropy in their strength is not enough for the layers to hold the load when weaker layers fail in many stacking sequences. For the case of PLA there must be at least the same number of layers aligned with the load as the number with a different raster angle. Even in those cases, progressive failure is only observed for high values of the raster angle, when the weaker layers fail due to matrix failure.

The best parts will be achieved by aligning the fibers with the highest component of the external load. When both components have the same sign, if the transverse direction does not fail, the interaction between the stresses will have a strengthening effect on the parts.

The failure criterion developed by Osswald and Osswald [7] is capable of characterizing failure of the parts capturing the interactions between all the stresses. With experimental tests, it can be implemented to simulation software to determine a safety region for the stress states.

## 6. References


1. Goncalves, J., et al., *Electrically Conductive Polyetheretherketone Nanocomposite Filaments: From Production to Fused Deposition Modeling.* Polymers (Basel), 2018. **10**(8).
2. Rinaldi, M., et al., *Additive layer manufacturing of poly (ether ether ketone) via FDM.* Composites Part B: Engineering, 2018. **145**: p. 162-172.
3. Gebisa, A.W., *Influence of 3D Printing FDM Proce.* 2019.
4. Wu, W., et al., *Influence of Layer Thickness and Raster Angle on the Mechanical Properties of 3D-Printed PEEK and a Comparative Mechanical Study between PEEK and ABS.* Materials (Basel), 2015. **8**(9): p. 5834-5846.
5. Wang, P., et al., *Effects of printing parameters of fused deposition modeling on mechanical properties, surface quality, and microstructure of PEEK.* Journal of Materials Processing Technology, 2019. **271**: p. 62-74.
6. Gebisa, A.W. and H.G. Lemu, *Investigating Effects of Fused-Deposition Modeling (FDM) Processing Parameters on Flexural Properties of ULTEM 9085 using Designed Experiment.* Materials (Basel), 2018. **11**(4).
7. Osswald, P.V. and T.A. Osswald, *A strength tensor based failure criterion with stress interactions.* Polymer Composites, 2018. **39**(8): p. 2826-2834.
8. Gol'denblat, I.I. and V.A. Kopnov, *Strength of glass-reinforced plastics in the complex stress state.* Polymer Mechanics, 1965. **1**(2): p. 54-59.

# Table of contents

***Chapter 1. Introduction*** ..... ***7***

***Chapter 2. State of the art*** ..... ***9***

2.1 Definitions and introduction of concepts ..... 9

*2.1.1 Additive manufacturing* ..... *9*

*2.1.2 Composites* ..... *14*

2.2 Literature review ..... 17

***Chapter 3. Project definition*** ..... ***23***

3.1 Motivation ..... 23

3.2 Objectives ..... 23

3.3 Code simulation ..... 24

*3.3.1 Algorithms* ..... *24*

*3.3.2 Data* ..... *31*

3.4 Failure characterization ..... 34

*3.4.1 Failure criterion* ..... *34*

*3.4.2 Material and testing* ..... *39*

***Chapter 4. Analysis of results*** ..... ***43***

4.1 CLT analysis ..... 43

*4.1.1 Uniaxial load* ..... *43*

*4.1.2 Biaxial load* ..... *49*

*4.1.3 Effect of yielding in the second direction* ..... *51*

4.2 Failure surface ..... 52

*4.2.1 Interaction* $\boldsymbol{\sigma 11 - \sigma 22}$ ..... *53*

*4.2.2 Interaction* $\boldsymbol{\sigma ii - \tau 12}$ ..... *54*

*4.2.3 3D Failure surface* ..... *56*

***Chapter 5. Conclusions and future work*** ..... ***57***

5.1 Conclusions ..... 57

5.2 Recommendations for future work ..... 58

***Chapter 6. Bibliography*** ..... ***59***

***ANNEX I*** *63*

CLASSICAL LAMINATION THEORY ..... 63

***ANNEX II*** *67*

SUSTAINABLE DEVELOPMENT GOALS..... 67

# List of figures

Figure 1: Schematic of Fused Filament Fabrication ..... 7
Figure 2: Additive manufacturing technologies [11] ..... 9
Figure 3: Selective laser sintering schematic [13] ..... 10
Figure 4: Laminated Object Manufacturing [15] ..... 11
Figure 5: Schematic of fused filament fabrication [16] ..... 13
Figure 6: Illustrations of the infill pattern, air gap and overlap ..... 13
Figure 7: Classification of composite material systems [17] ..... 15
Figure 8: Levels of observation and types of analysis for composite materials [17] ..... 17
Figure 9: FFF printing parameters. Single layers with 0º,90º and 45º raster angle. ..... 18
Figure 10: Flowchart for determination of the maximum load with FPF and LPF conditions ..... 26
Figure 11: Stress strain relationship for PLA[34] ..... 27
Figure 12: Flowchart for determination of the FPF accounting for the effect of yielding in the second direction ..... 30
Figure 13: Stacking sequences. Top: $[\theta]_4$, $[\pm\theta]_s$. Bottom: $[0,\pm\theta]_s$, $[0,\pm\theta,0]_s$ ..... 33
Figure 14: Stress components on a representative element ..... 35
Figure 15 Schematic of the slope in $\sigma_{22}$-$\tau_{12}$ plane [28] ..... 36
Figure 16: Tensile, compressive and torsion specimens with respective bead orientation in the gauge section [28] ..... 40
Figure 17: PLA $[\theta]_4$ maximum load over height vs raster angle ..... 43
Figure 18: PLA $[0, \pm\theta]_s$ maximum load over height vs raster angle ..... 46
Figure 19: E-glass/ Epoxy [0, ±θ]s maximum load over height vs raster angle ..... 46
Figure 20: PLA [0, ±θ,0]s maximum load over height vs raster angle ..... 48
Figure 21: E-glass/ Epoxy [0, ±θ,0]s maximum load over height vs raster angle ..... 48
Figure 22: PLA [ ±θ]s under biaxial load ..... 49
Figure 23: E-glass/Epoxy [ ±θ]s under biaxial load ..... 50
Figure 24: Comparison of PLA $[\pm\theta]_4$ with and without accounting for the yielding effect ..... 51

Figure 25: Failure envelope in the axial stress plane $\sigma_{11}$-$\sigma_{22}$ ..... 53
Figure 26: Failure envelope in the shear axial stress plane $\sigma_{11}$-$\tau_{12}$ ..... 55
Figure 27: Failure envelope in the shear axial stress plane $\sigma_{22}$-$\tau_{12}$ ..... 55
Figure 28: 3D failure surface for CF nylon ..... 56
Figure 29 Positive $\theta$ ..... 64
Figure 30 Laminate with coordinate notation of individual plies ..... 65
Figure 31 Force and moment resultants ..... 65

# *List of tables*

Table 1: PLA mechanical properties for different raster angles [25] ..... 31
Table 2: PLA Parameters [25] ..... 32
Table 3: E-glass/Epoxy properties [17] ..... 32
Table 4: Interaction stress components ..... 36
Table 5: Tensorial components ..... 37
Table 6: Recommended printing parameters ..... 39
Table 7: Estimated strength parameters for CF nylon ..... 42
Table 8: Numerical values for the failure function coefficients ..... 52

# Chapter 1. INTRODUCTION

Additive manufacturing (AM) is a promising technique for both rapid prototyping and fabricating functional parts. Parts are formed layer by layer from a three-dimensional computer aided design (CAD) model. The main advantages of AM involve the creation of complex shapes. This would otherwise be impossible for traditional manufacturing techniques, without the need of expensive tooling or molds.[1, 2] It also reduces the cycle time and the cost of product development and enables the use of multiple materials in the same part.[3, 4] AM technologies are particularly suitable for printing fully functional systems, mass customization, decentralized and on-demand manufacturing. Some applications include healthcare, automotive, aerospace and electronics.[1, 3-5]

Most popular AM processes are Selective Laser Sintering (SLS), Stereolithography (SLA) and Fused Deposition Modeling (FDM®) or Fused Filament Fabrication (FFF).

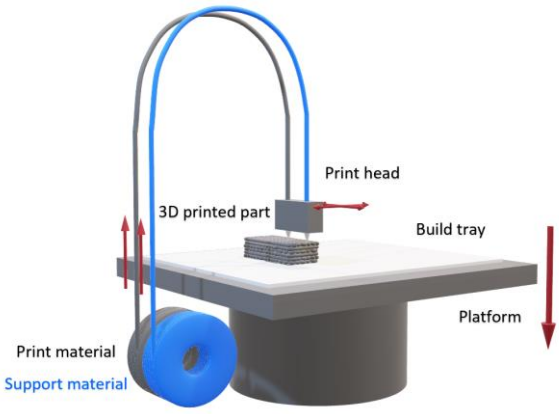


*Figure 1: Schematic of Fused Filament Fabrication*

FFF is the most mature, popular, and fastest growing of all the techniques.[6] As shown in Figure 1, a melted filament of a thermoplastic material is extruded and

deposited on a heated bed to form the final geometry. 3D-printers can be separated based on the type of materials extruded: consumer and professional printers. Consumers use low melting temperature polymers like poly lactic acid (PLA), acrylonitrile butadiene styrene (ABS), polyethylene terephthalate glycol modified (PETG), Nylon and polycarbonate (PC) due to their low cost and ease of use. Professional printers require higher temperatures for high performance polymers: polyaromatics like polyetheretherketone (PEEK), polyaryletherketone (PAEK), polyetherketoneketone (PEKK), ULTEM, and polyurethane (PU).[7] The addition of a reinforcement material, like carbon fiber, can improve mechanical properties and thermal stability of these polymers.[1]

Mechanical properties of printed parts are highly dependent on the processing parameters.[8] Structural parameters, such as fiber orientation or length, have the greatest influence on the final properties but processing parameters, printing temperature or speed, also have a significant influence.[9] Optimizing these parameters allows to control mechanical properties.

# Chapter 2. STATE OF THE ART

## 2.1 DEFINITIONS AND INTRODUCTION OF CONCEPTS

### 2.1.1 ADDITIVE MANUFACTURING

There are seven types of technologies that can be used for additive manufacturing. These are powder bed fusion, directed energy deposition, sheet lamination, binder jetting, material jetting, material extrusion and vat photopolymerization[10]. Figure 2 illustrates these methods.

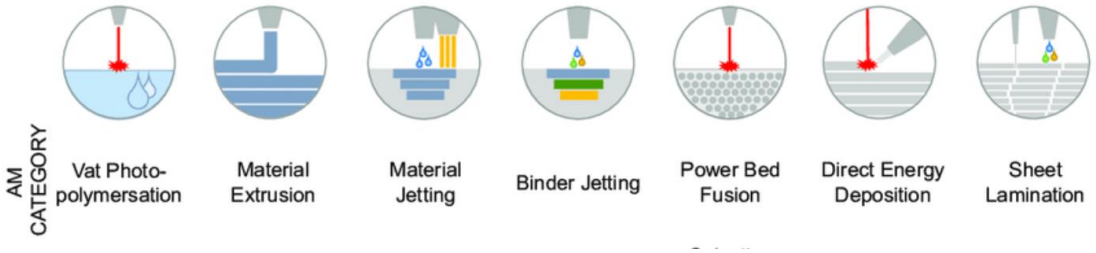


*Figure 2: Additive manufacturing technologies [11]*

#### *2.1.1.1 Powder bed fusion*

Powder bed fusion is used in selective laser sintering (SLS) printers. An energy source, such as a laser or an electron beam, selectively fuses an area of a powder bed to form one layer. Once the layer is finished, the surface is covered in powder again and leveled to form the following layer. A schematic of this process is shown in Figure 3. This method of printing allows the creation of complex geometries without the need of additional support material. The powder that is not melted while forming the final geometry remains loose and it can act as a base for the overhangs or fragile features of the design. In general, polymers, metals, ceramics, and composites are suitable materials for this method. It must be possible to melt and re-solidify the material.[12]

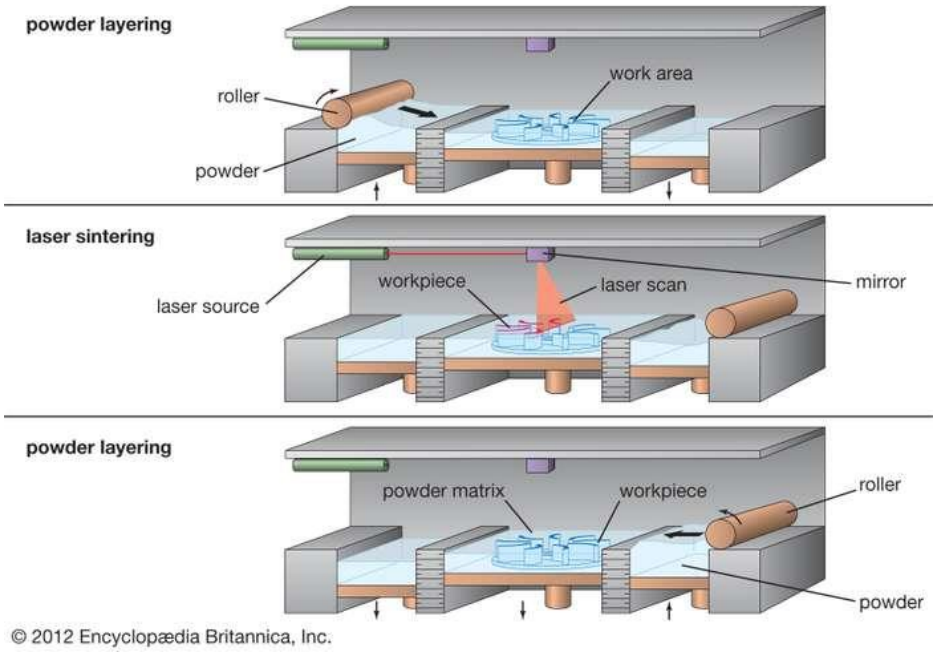


*Figure 3: Selective laser sintering schematic [13]*

### *2.1.1.2 Binder jetting*

Binder jetting also starts from powder material to form the final geometry. Similarly, once a layer is created, more powder is spread and leveled with a roller to continue with the process. For this method, instead of melting the material, a nozzle ejects droplets of binder that hold the powders together. Once the part is fully printed, it is normally left in the powder bed for some time to allow the binder to set. Afterwards, the unbounded powder is removed, and it is ready for post- processing treatments. The part can be sintered or infiltrated to impart desired mechanical properties. Suitable materials are polymers, ceramics, metals, and composites.[12]

### *2.1.1.3 Direct energy deposition*

Direct energy deposition creates the parts by melting the material as it is being deposited. It is principally used for metals, although it can also work for other materials. A melt pool is formed on the substrate with a laser beam, powder is fed into the pool and it melts forming a deposit that is fused to the previous layer.[14]

### 2.1.1.4 Sheet lamination

The material in sheet lamination-based systems starts from a solid sheet. Each layer is cut to an outline that corresponds to the design cross section, then the layers are stacked and bonded to form the solid model. A variation for this process is stacking the layers first and then cutting them. It can be subdivided by the type of bonding used between the sheets, namely gluing or adhesive bonding, thermal bonding, clamping, and ultrasonic welding [12, 14]. The process is illustrated in Figure 4.

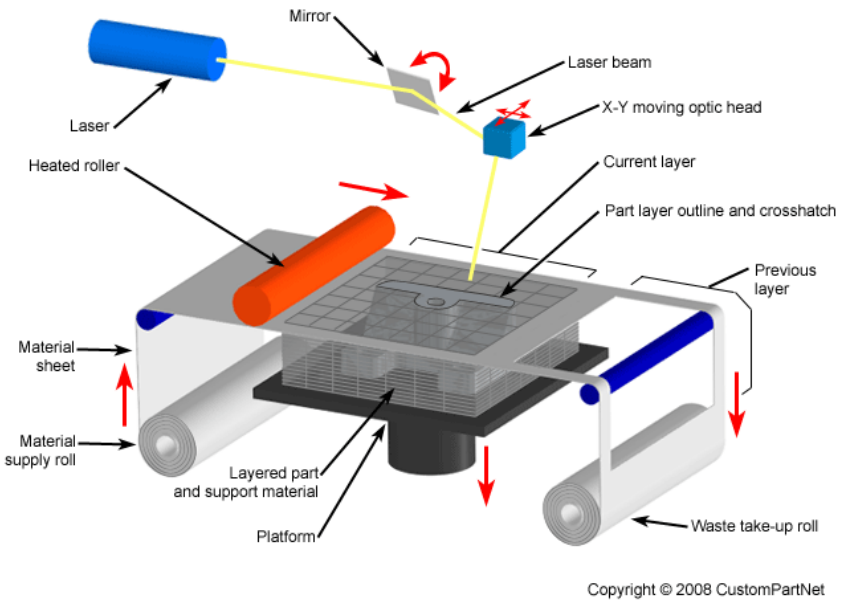


*Figure 4: Laminated Object Manufacturing [15]*

### 2.1.1.5 Vat photopolymerization

Stereolithography (SLA) uses the vat photopolymerization technology. The process is very similar to powder bed fusion technologies, but instead of powder, the material starts in liquid state. A vessel with a photosensitive polymer is the recipient for a platform where each layer is cured with a laser. When a layer is completed the platform is lowered by a distance equal to the layer thickness and a recoating blade is passed over the liquid to ensure an even level on the surface. The liquid does not provide any support for the overhanging features of the geometry; therefore an

additional structure or web must be used to ensure accuracy in the final dimensions.[14]

#### *2.1.1.6 Material jetting*

Material jetting is used in Droplet Deposition Manufacturing. Small droplets of melted material are placed on the previous layers to build the part. Similar to the previous method, complex geometries require an external support. This support can be printed with a second nozzle and a different material and removed after the design is completed. The material must be melted just above its melting temperature in order to solidify immediately after it is deposited to avoid distortion. This requirement limits the materials that can be used to thermoplastic polymers or wax.[14]

#### *2.1.1.7 Material extrusion*

This technology is the leading method of all additive manufacturing techniques. In Fused Filament Fabrication (FFF), bulk material is heated inside a portable chamber and extruded through a nozzle. A schematic of this process is depicted in Figure 5. The raster dimensions will be constant if both the pressure applied and the printing velocity are kept constant. Like in material jetting, the material must solidify immediately after it is deposited, and it must also bond to the previous layer. This can be achieved either relying on thermal effects, in the case of FFF once it is printed, the room temperature will solidify the material; or with a chemical change to cause the solidification. A curing agent, a reaction with air or a residual solvent will ensure the bonding in those cases.

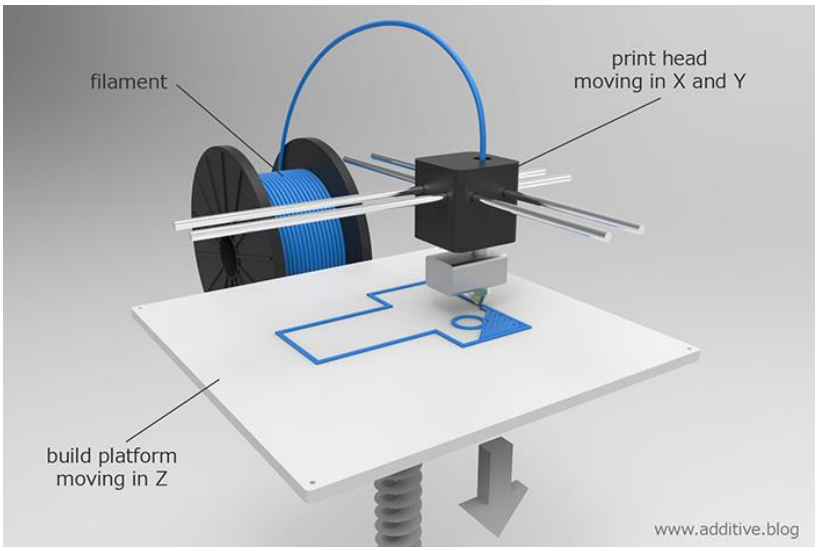


*Figure 5: Schematic of fused filament fabrication [16]*

To ensure dimensional accuracy, the outline material is plotted first. This raster will act as a border to constrain the fill material. The starting point in each layer must be carefully chosen because a seam will form if the starting point coincides in all the layers. Since the extruded filament has a finite dimension, if the software sets the starting and stopping point in the same coordinates, overlapping will occur. It is very difficult to control the flow precisely, nevertheless a slight overlap is more desirable than an air gap at this point. The extrusion could start at different points in each layer to avoid the seam or it could be removed with a post processing treatment.

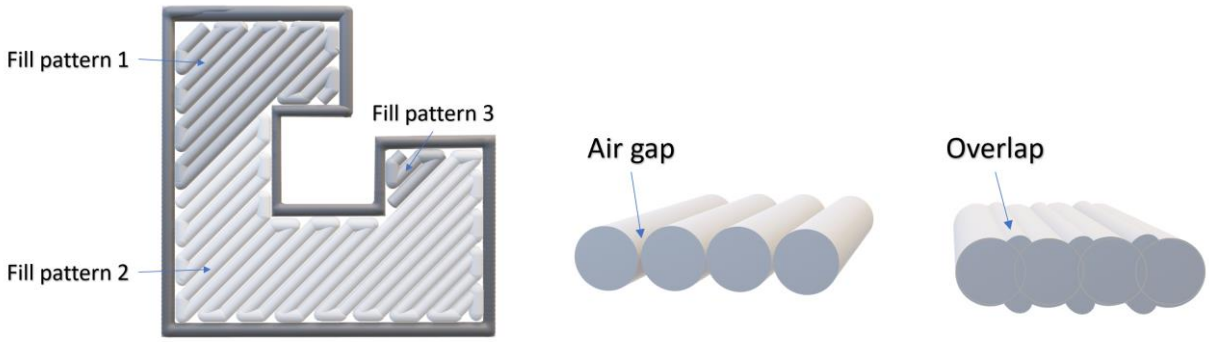


*Figure 6: Illustrations of the infill pattern, air gap and overlap*

Regarding the infill, the first consideration to be made is the determination of an adequate offset to deal with overlapping of the beads. Secondly, the design of the optimal infill pattern is difficult to do. There are many possibilities for the trajectory of the pattern, there is not a single solution for every cross section. Besides, it may not be possible to fill one layer with a continuous filament in complex geometries. In that case, broken trajectories will be necessary for the particular shape. In the geometry shown in Figure 6, three patterns are needed to fill the layer. Even considering a simple outline, for example a circle, each layer could be filled in a circular motion either from the center or starting from the outside. Furthermore, the stacking of the subsequent layers will play a major role in the part's strength. If the same pattern is repeated in all the layers the paths will be placed exactly above each other. This will result in anisotropic parts due to the directionality in the fibers. For this reason, the properties will be more similar in the different directions if a crossing pattern is used. Many changes in direction will be needed to fill the outline perimeter. The edges of the beads are areas which will also be prone to void formation and overlapping.

It is clear that precise control of the extrusion is crucial for a successful print. It depends numerous parameters, for example, the input pressure, the temperature, the nozzle diameter, or the material characteristics. These parameters should be carefully chosen for each application.[12]

### 2.1.2 COMPOSITES

Composite materials are a heterogeneous mixture of two or more distinct phases that contribute to the overall mechanical performance. The matrix is the continuous phase, it is weaker and less stiff, and the reinforcement is stiffer and stronger, it is normally a discontinuous phase.

The composite properties depend on the constituents, the distribution and geometry of the phases. The volume fraction is one of the most important parameters, a higher volume of the reinforce material will provide stronger composites. However, it is not

the only parameter that governs the final properties. For example if the reinforcing material shows directionality, the composite will be highly anisotropic. On the contrary if the reinforcement is randomly distributed the composite will be more isotropic.

The composites that only have two phases can be classified depending on the type, geometry, and orientation of the reinforce material into three categories, as illustrated in Figure 7.

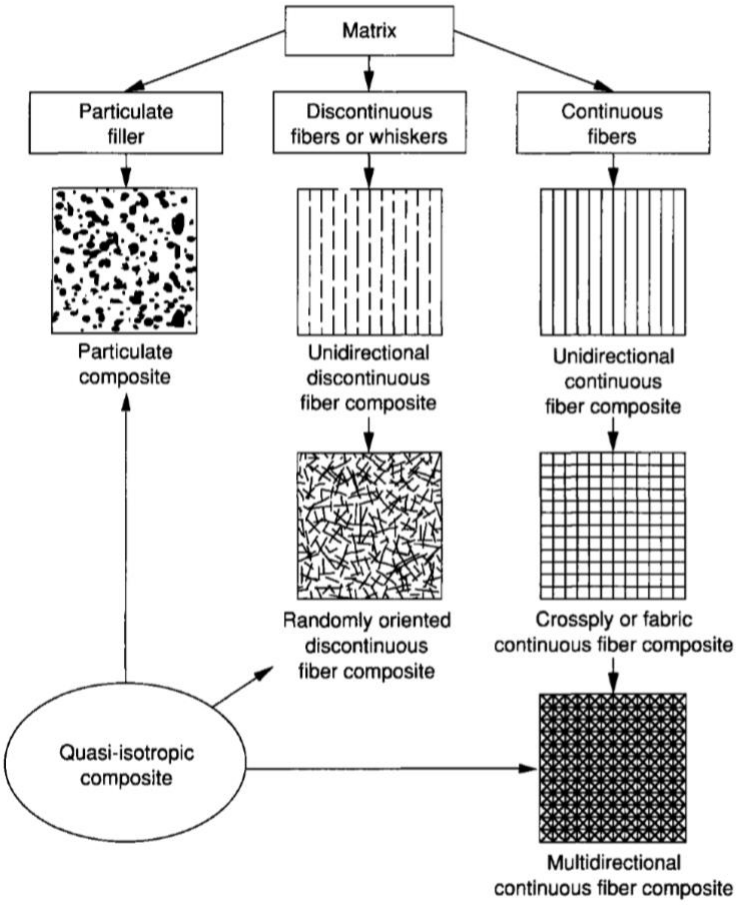


*Figure 7: Classification of composite material systems [17]*

Particulate filler composites have the reinforcement in the shape of small particles randomly distributed.

Discontinuous fiber composites have short fibers to strengthen the matrix. The short fibers can either be unidirectionally oriented or randomly oriented.

Continuous fibers composites have continuous fibers embedded in their matrix. They can be all in the same direction or with different orientations.

Particulate filler and discontinuous fibers composites will achieve low- to medium-performance composites. In these cases, the reinforcing material will provide some stiffening but a limited strengthening effect. The strength will be a matrix dominated property since this phase is going to hold the load. Particulate composites and randomly oriented discontinuous fiber composites will exhibit quasi-isotropic properties on a macroscopic scale while the orientation of the short fibers in unidirectional discontinuous fiber composites gives them preferable directions in their properties.

High performance composites will be achieved with continuous fiber reinforcements. The matrix no longer holds the load; its role is to protect the fibers, provide bonding and support, and locally transfer stresses from one fiber to another. In the direction of the fibers, the reinforcement material will dominate the strength, while the transverse direction will be matrix dominated and thus significantly weaker. If all the fibers are all aligned in the same direction the properties will be highly anisotropic.

Composites can also be classified on the type of material used for the matrix. There are polymer-, ceramic-, metal- and carbon-matrix composites. Their use is determined by the temperature requirements.

Based on the level of observation, different approaches are used to study the mechanical performance of composite materials. Micromechanics describes the properties of a lamina from the matrix and fiber characteristics. A stack of laminae forms a laminate, and the relation between them is studied by macromechanics. Lastly, structural analysis relates the laminates with the loads applied on a structure.

Figure 8 shows the different levels of observation and the types of analysis that were explained.[17]

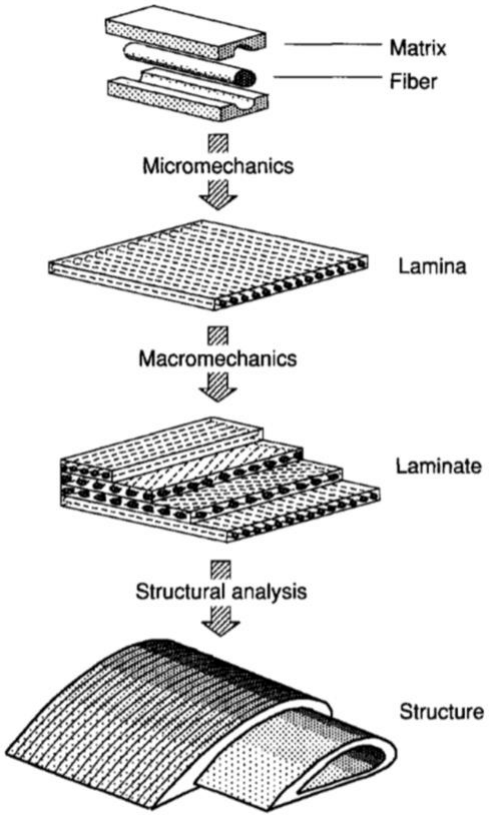


*Figure 8: Levels of observation and types of analysis for composite materials [17]*

## 2.2 LITERATURE REVIEW

Parts created by FFF are made of layers of oriented filaments, as shown in Figure 9, resulting in direction dependent mechanical properties. In particular, FFF parts with all filaments printed in a direction exhibit orthotropic properties. Given their complex behavior, modelling mechanical performance of FFF parts is essential for designing functional parts. However, the two main problems are the lack of constitutive relationships and models to predict their strength and failure loads.

Mechanical assessment of FFF structures has been primarily conducted experimentally hence the existing models are only valid for a particular material and the FFF processing parameters that are used, but general trends can be inferred from the results. The following papers summarize the research that studied these relations for pure thermoplastic polymers.

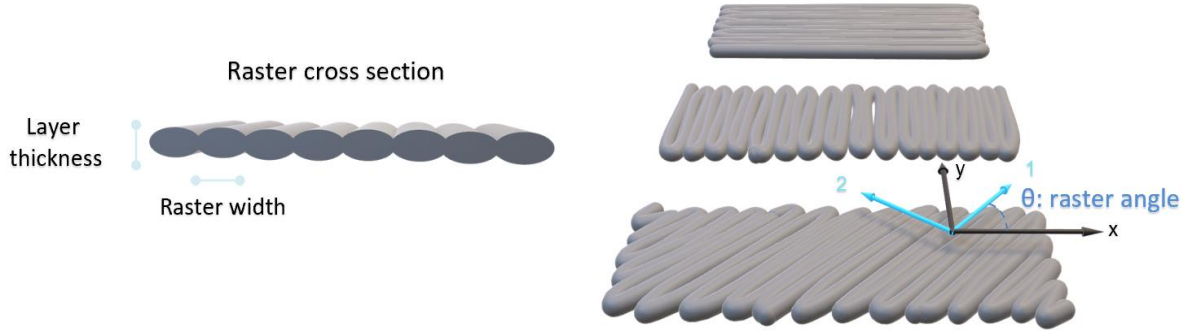


*Figure 9: FFF printing parameters. Single layers with 0º,90º and 45º raster angle.*

Rankouhi et al.[18] studied the influence of layer thickness and raster orientation on ultimate tensile strength and the elastic modulus of 3D printed ABS. Smaller layer thickness yielded stronger parts. Their conclusion was that this happened because of lower air gaps, as evident from their cross-sectional micrographs. Aligning filaments with the loading direction gives higher strength. Similar research was performed by Wu et al. [4], where they investigated the effects of layer thickness and raster orientation on ABS and PEEK and compared it to the properties of the injection molded materials. The reduction of the performance of PEEK was more significant than for ABS. In this case, the best properties were not reported for the minimum layer height, but a local maximum was observed. The need of reducing pore (air gap) formation and improving interlayer bonding was assumed to govern the performance of FFF printed parts. Chacon et al.[19] studied layer thickness, build orientation and extrusion rate on PLA with a low cost printer. In this paper, for higher strength, the best layer thickness was found to be conditioned by the build orientation. For upright built pieces larger layer thickness yielded better results while

for on-edge and flat orientation the different layer thicknesses only made a slight difference on the final properties. The build orientation has the greatest influence on the final properties and the failure mode. For upright printed samples, the load is transversely carried by the piece, interlayer failure was observed, and this was the weakest direction. On-edge and flat samples present similar behavior, their strength and stiffness are higher than upright samples and have a ductile fracture mode. Effects of layer thickness, raster angle and raster width on PLA part properties were also investigated by Rajpurohit and Dave [20]. They concluded the tensile properties were conditioned by raster angle, raster width, and the interaction between layer thickness and raster width. Aligning the filaments with the load showed best tensile results, which is achieved with a raster angle of 0º.

The addition of fibers of a reinforcing material can improve the mechanical properties of the printed parts. Ning et al.[21] studied the effect of raster angle, infill speed, nozzle temperature and layer thickness on tensile properties for carbon fiber reinforced ABS. As for pure polymers, aligning the load with the raster angle yields higher strengths. The tensile properties first increased with temperature until an inflection point was reached. They concluded that lower temperatures prevent a strong bonding between rasters while more pores are formed at higher temperatures, both of which lead to a decrease in tensile properties. Justo et al.[22] compared the performance of printing versus autoclave manufacturing for long fiber reinforced polymers. The properties of the printed parts were significantly lower due to the porosity formed, however, in comparison with the pure polymer there is a major improvement because of the addition of the reinforcing material. In the research of Tekinalp et al.[23] the mechanical properties of short carbon fiber reinforced ABS were investigated. They tested and compared additive manufactured and compression molded parts. The 3D samples had highly oriented short fibers, they were almost perfectly aligned with the beads, but had higher porosity than compression molded specimens. The fibers in compression molded specimens were more disperse but they did not have voids. These last parts were

stronger, showing that pore formation is the dominant phenomenon in the strength reduction.

Along with these experimental investigations, analytical and semi-analytical methods have also been used to model mechanical behavior from a theoretical approach. These approaches are either based on the classical laminate theory (CLT) or micromechanics.

For fully filled parts, the structure of FFF parts resembles a laminated composite. Therefore, the CLT may be applied to model their mechanical response. Each layer of the structure is treated as a lamina and the whole piece would be the laminate. The main disadvantages of this approach are the need of characterization of the mechanical constants and the restriction to parts with 100% infill.

Li et al.[24] characterized the mechanical constants of ABS via tensile testing. The elastic modulus and the maximum stress were measured for the first and second direction from uniaxial tensile testing of samples with 0º and 90º raster angle, respectively. The shear modulus as well as the ultimate shear stress are not directly measured but they can be calculated from a sample with 45º raster angle. Empirical parameters were also used to account for void density and confirmed with cross sectional microscopy of the samples. Their model was then used to predict the behavior of cross-ply laminates, with good agreement between the theoretical values and those measured. Casavola et al.[25] followed a similar methodology to characterize the same constants for ABS and PLA. In this case, void density was not considered, but their model reported errors lower than 6.6 % for the estimation of the elastic modulus of laminates with a symmetric and balanced stacking sequence. Somireddy et al.[26] studied unidirectional and bidirectional laminates of ABS with two different layer thicknesses. The constants were first measured with unidirectional samples and the CLT model validated with the bidirectional laminates. They observed that layer thickness and lay-up had a more significant effect on tensile properties of unidirectional samples and on the flexural properties of bidirectional samples. The influence of filament dimensions and chemical

composition on ABS printed samples was studied by Alaimo et al.[27] They concluded that CLT and Tsai-Hill yielding criterion were capable of correctly estimating in-plane stiffness and strength. Mazzei Capote et al. [28, 29] developed an interactive failure criterion. Tensile, compressive, and torsion tests were performed to investigate the relation between shear, tensile and compressive stresses. Their model was able to correctly predict failure, it was later validated with a test set in another study. Lastly, Yao et al.[30] investigated interlayer failure and developed a strength model based on the fourth stress invariant. Their basic hypothesis was that tensile normal stress and shear stress at the boundary of two filaments are the cause for interlayer failure.

The micromechanics approaches of repeating unit cells assume filament rasters are perfectly bonded. In the research done by Croccolo et al.[31], the load required to break samples with a 45º raster angle is calculated addressing the effect of contours. An advantage of AM is the ability to reduce weight by creating partially filled structures. This micromechanics approach enables the analysis of these structures and can be used to derive expression for the structure-property relationships.[32]

Finally, computational methods are a powerful tool for stress analysis in complex structures. Finite element analysis (FEA) has been used not only to predict the properties of the printed parts but also to simulate the printing process. The research done using these models is extensive [9] and has been used with different objectives. In line with the current investigation, Rodriguez et al.[33] developed a mathematical model to optimize printing parameters to maximize the stiffness and strength of the printed parts under certain loading conditions.

# Chapter 3. PROJECT DEFINITION

## 3.1 MOTIVATION

Fused Filament Fabrication is a promising technique for both rapid prototyping and the creation of functional parts. As previously explained, the parts are highly anisotropic, their properties are direction dependent. By adjusting the processing parameters, the final properties can be locally controlled, and the performance of the parts improved. Developing computational algorithms to optimize them is essential to save time and materials on performing tests for every possible permutation. Previous research has proven CLT to be a good approach for modeling solid FFF parts, it is therefore a valid model to predict their mechanical behavior and to determine the best value for some processing parameters.

## 3.2 OBJECTIVES

- Comparison of the first ply failure (FPF) vs the last ply failure (LPF).

  The first ply failure considers that the part has failed when the first layer breaks while for the last ply failure this happens when the last layer breaks. Due to the difference in the strengths between the first and second principal directions, a progressive failure in the parts may be observed.

- Study the effect of yielding in the second direction on the laminate.

  The layers loaded transversely yield before their failure. The effect of this phenomenon will be analyzed.

- Angle optimization for different stacking sequences under representative mechanical loadings.

When the parts are subject to combined stresses, the raster angle can be optimized to achieve stronger structures.

- Characterization of failure for carbon fiber- nylon FFF printed parts.

  A strength tensor-based criterion with stress interaction will be calculated for carbon fiber- nylon material.

## *3.3 CODE SIMULATION*

### 3.3.1 ALGORITHMS

A general load is applied to different stacking sequences to determine the failure load and optimize the raster angle. The equations used in the code presented below are explained in

ANNEX I.

The code follows the next steps:

1. Enter material constants and stacking sequence
2. Calculate reduced stiffness matrix [Q], transformation matrix [T] and transformed reduced matrix [Qxy] at each layer.
3. Calculate laminate stiffness matrixes (A, B and D) and the inverse [abd].
4. Enter mechanical loadings [N]xy and [M]xy.
5. Calculate the reference plane strains [$\varepsilon_0$] and laminate curvatures [$\kappa$].
6. Calculate the strains at each layer $[\varepsilon]_{xy}^{k}$ . The coordinates $z_k$ and $z_{k-1}$ are used to calculate the strains at the top and the bottom of each lamina, the extreme values for the strains.
7. Transform the stresses to the local coordinates in each lamina $[\varepsilon]_{12}^{k}$
8. Calculate the stresses in the local axes $[\sigma]_{12}^{k}$
9. Enter the maximum strengths in the principal directions $F_t$, $F_c$, S
10. Compute safety factors of each lamina $S_f^k$
11. 
    a. Determine the lamina with the minimum safety factor $k_i$
    b. Calculate the load required to break the lamina with the minimum safety factor.
12. Question whether it is the first lamina to fail (i=1)
    a. If the answer is yes, the maximum load to break the first ply is $[NM]_{FPF}=S_f^k\ [NM]$
13. If the answer to the above question is no, check if the LPF condition is met.
14. If the condition is not met, identify the failure mode of the $k_i$ lamina to discount. Question whether it is fiber failure or matrix or interfiber failure.
    a. If $\left(\frac{\sigma_2^k}{F_2}\right)^2+\left(\frac{\tau_{12}^k}{S}\right)^2<\left(\frac{\sigma_1^k}{F_1}\right)^2$ the lamina failed due to fiber failure. Update the stiffness in the first direction ($E_1^k=0$) and repeat from the step 2.

b. If $\left(\frac{\sigma_2^k}{F_2}\right)^2 + \left(\frac{\tau_{12}^k}{S}\right)^2 > \left(\frac{\sigma_1^k}{F_1}\right)^2$ the lamina failed due to matrix or interfiber failure. Update the stiffness in the second direction ($E_2^k=0$) and the shear modulus ($G_{12}^k=0$) and repeat from the step 2.

15. If the condition in step 13 is met, the maximum load to break the last ply is $[NM]_{LPF}=S_f^k$ [NM]

Figure 10 in the next page is a flowchart with the steps followed.

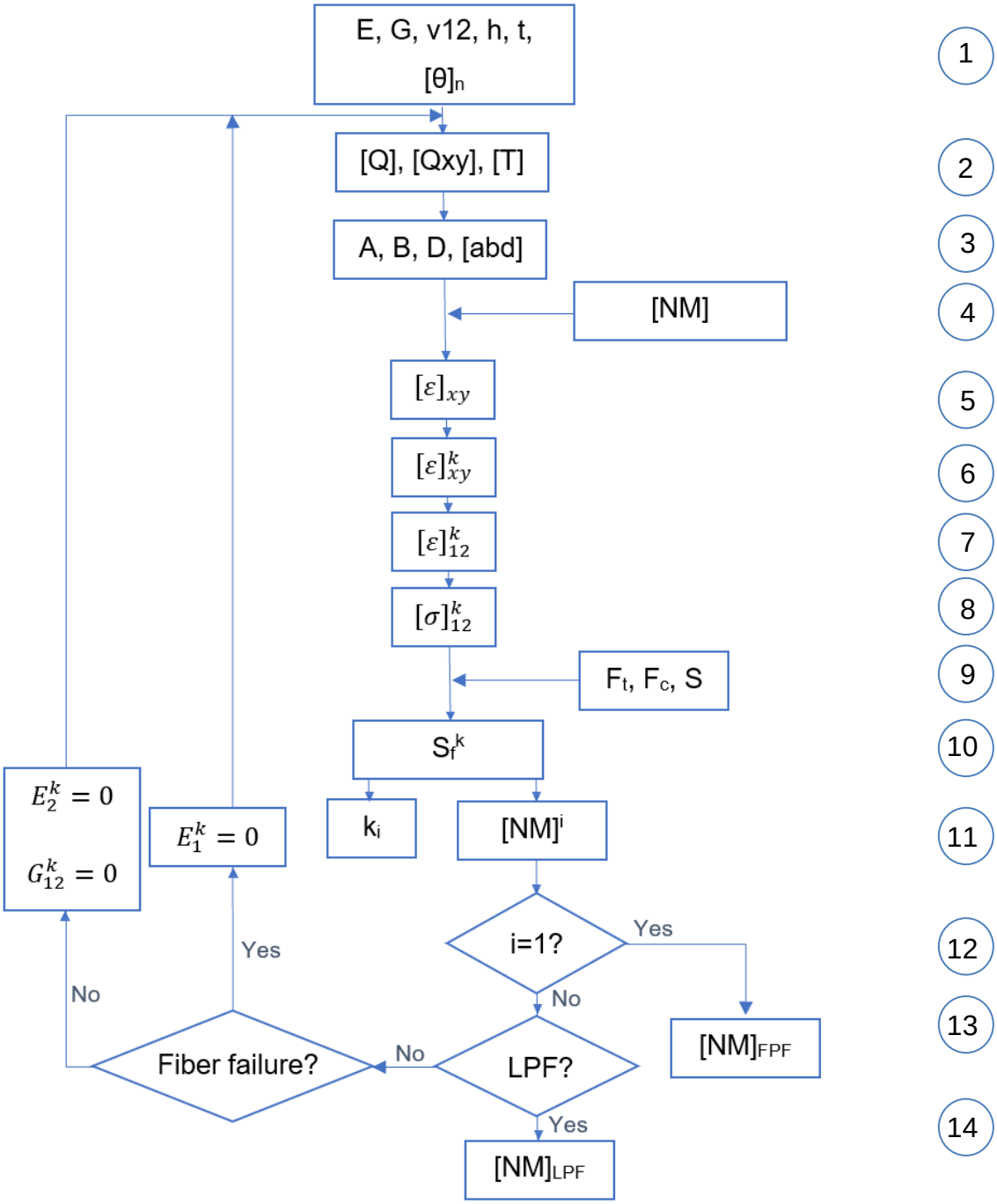


*Figure 10: Flowchart for determination of the maximum load with FPF and LPF conditions*

Looking at the stress-strain relationship from uniaxial tensile tests, different behaviors can be observed in the first and second principal directions. The layers with 90º raster angle yield at lower strains than the layers with filaments aligned with the load. Once they have yielded their stiffness drops significantly but they can still hold load since they have not failed yet.

The mechanical properties in the second direction are lower, therefore laminae will yield before the laminae in the first direction, as it can be seen in Figure 11.

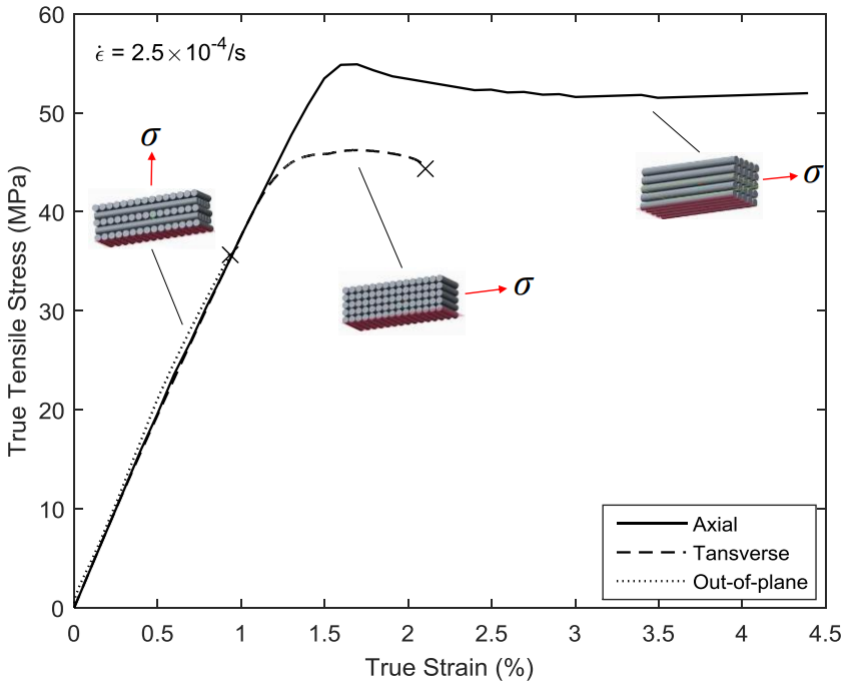


*Figure 11: Stress strain relationship for PLA[34]*

The stress-strain relationship in the second direction is no longer linear. The model must be modified to account for this effect. Although the plastic region follows Hollomon's law it was approximated by a linear relationship. The material starts with a high elastic modulus and once it yields the modulus drops to a low value. The

yielding point was determined when the deformation reached the strain at yielding in the second direction.

To determine the load required for failure, with two linear relationships, the principle of superposition can be applied. The total load will be the summation of the load required for yielding plus the maximum load that the layers can hold afterwards.

To study the effect of yielding in the second direction, the following algorithm was developed.

1. Enter material constants and stacking sequence
2. Calculate reduced stiffness matrix [Q], transformation matrix [T] and transformed reduced matrix [Qxy] at each layer.
3. Calculate laminate stiffness matrixes (A, B and D) and the inverse [abd].
4. Enter mechanical loadings [N]xy and [M]xy.
5. Calculate the reference plane strains [$\varepsilon_0$] and laminate curvatures [κ].
6. Calculate the strains at each layer $[\varepsilon]_{xy}^{k}$ . The coordinates $z_k$ and $z_{k-1}$ are used to calculate the strains at the top and the bottom of each lamina, the extreme values for the strains.
7. Transform the stresses to the local coordinates in each lamina $[\varepsilon]_{12}^{k}$
8. Calculate the stresses in the local axes $[\sigma]_{12}^{k}$
9. Enter the maximum strengths in the principal directions $F_t$, $F_c$, S
10. Compute safety factors of each lamina $S_f^k$
11. Calculate the maximum load to break the first lamina and repeat steps 5 to 7.
12. Compute $w = \frac{\varepsilon_{2y}}{[\varepsilon]_2^k}$ and question whether it is smaller than 1.
13. If the answer is yes:
    a. Steps 4 to 7 are repeated for w[NM], to calculate $[\varepsilon]_{12\_y}^{k}$
    b.
        i. The stiffness in the second direction for the laminae that yielded is updated to a new value. $E_2^k=E_2'$

ii. New compliance and stiffness matrixes are calculated [Q2], [abd2].

iii. Steps 4 to 10 are repeated to calculate $S_f^k{}_2$

14. Sum $[\varepsilon]^k_{12_y} + [\varepsilon]^k_{12_2} = [\varepsilon]^k_{12}$

15. Calculate $[\sigma]^k_{12} = [Q_{xy}][\varepsilon]^k_{12\_y} + [Q2_{xy}][\varepsilon]^k_{12\_2}$

16. If the answer to question in step 8 was no, set $S_f^k{}_2$ to 0 and w to 1

17. Calculate the safety factor $S_f^k = w\, S_f^k + S_f^k{}_2$

18. Find the load required to break the first ply $[NM]_{FPF}$

The flowchart for this algorithm is presented in Figure 12.

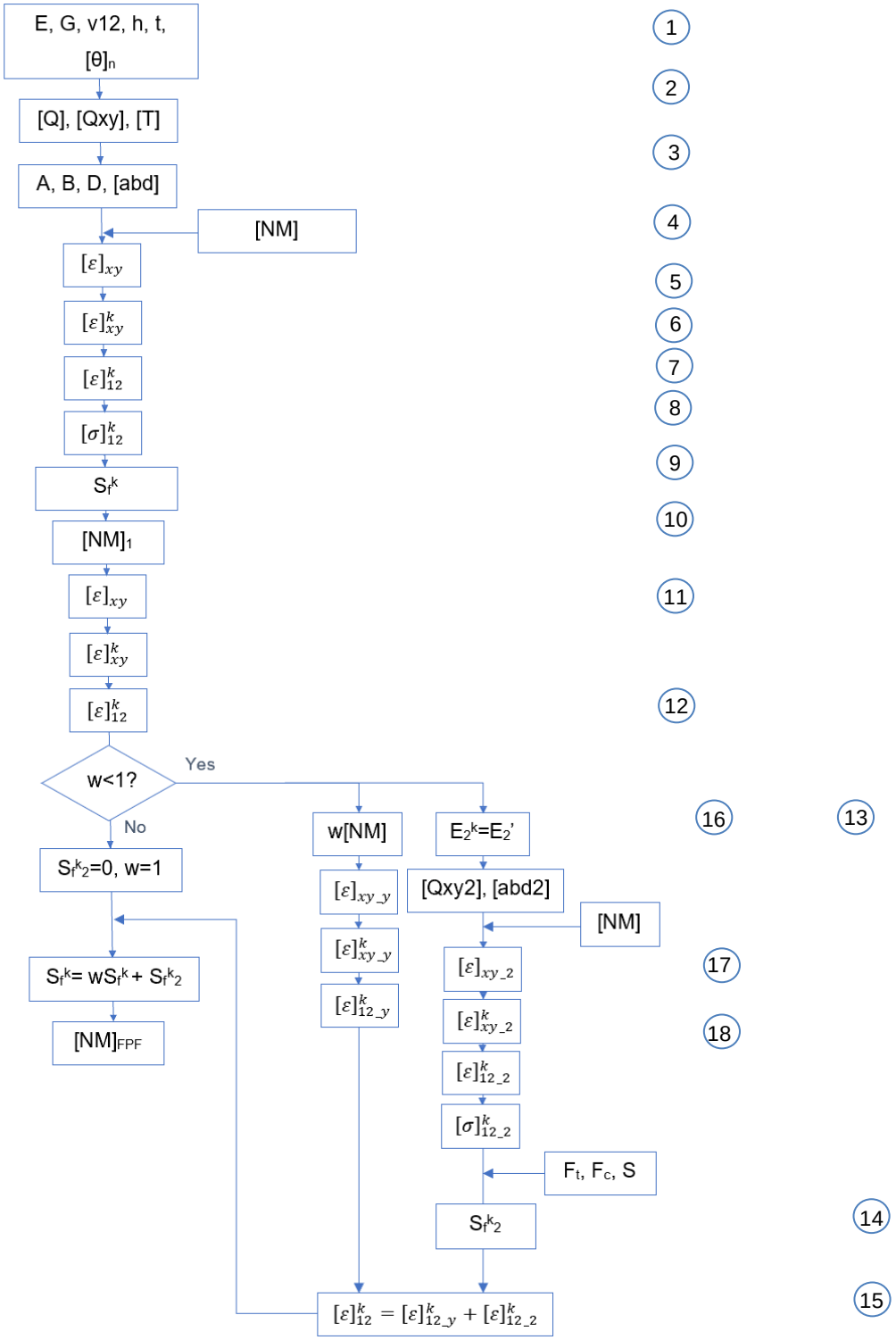


*Figure 12: Flowchart for determination of the FPF accounting for the effect of yielding in the second direction*

### 3.3.2 DATA

The material constants that were used are for PLA, experimentally measured by Casavola et al[25].

They conducted tensile experiments to determine Young's modulus, Shear modulus and ultimate tensile strength. The values reported are presented in Table 1.

*Table 1: PLA mechanical properties for different raster angles [25]*

| Specimen | Young's modulus [GPa] | Young's modulus Standard deviation [GPa] | UTS [MPa] | UTS Standard deviation [MPa] |
|---|---|---|---|---|
| **PLA 0°** | 3.12 | 0.03 | 50.23 | 0.77 |
| **PLA 45°** | 2.86 | 0.02 | 40.68 | 0.75 |
| **PLA 90°** | 2.77 | 0.32 | 22.49 | 6.7 |

The Young's modulus in the first and second direction are not significantly different, therefore a value of E= 3 GPa was used. The shear strength is reported to be $G_{12}$= 1246.57± 32.21MPa and the Poisson's ratio v12=0.330. The maximum tensile strength in the first direction is $X_t$=$UTS_{0^o}$=50.23 MPa, the maximum strength in the second direction is $Y_t$=$UTS_{90^o}$=22.49 MPa and the shear strength is S=22.25 MPa. This value was calculated with the following equation [30]:

$$S = \left( \frac{4}{UTS_{45º}^2} - \frac{1}{UTS_{0º}^2} \right)^{-\frac{1}{2}}$$

All the parameters are summarized in Table 2.

*Table 2: PLA Parameters [25]*

| | | | |
|---|---|---|---|
| $E_1$ | 3 GPa | $X_t$ | 50 MPa |
| $E_2$ | 3 GPa | $Y_t$ | 22 MPa |
| $G_{12}$ | 1.25 GPa | S | 22 MPa |
| $v_{12}$ | 0.33 | | |

The CLT was first developed for composites, therefore in the analysis the results are compared with continuous fiber E-glass/Epoxy composite, whose properties are presented in Table 3.

*Table 3: E-glass/Epoxy properties [17]*

| | | | |
|---|---|---|---|
| $E_1$ | 41 GPa | $X_t$ | 1140 MPa |
| $E_2$ | 10.4 GPa | $Y_t$ | 39 MPa |
| $G_{12}$ | 4.3 GPa | S | 89 MPa |
| $v_{12}$ | 0.28 | | |

The stacking sequences that are used for the analysis are shown in Figure 13.

The orientation of each layer of a laminate is indicated by a vector containing the order of the angles. The subscript of the vector indicates the number of times that the sequence is repeated.

The unidirectional laminate has four plies oriented with the raster angle. This stacking sequence is indicated by $[\theta]_4$, it has four layers.

The multidirectional laminates have four oriented layers. Two with a positive angle and two with a negative angle. The subscript ‘s’ indicates the sequence is repeated in a symmetric manner. Additional 0º raster angle layers were added as shown in Figure 13.

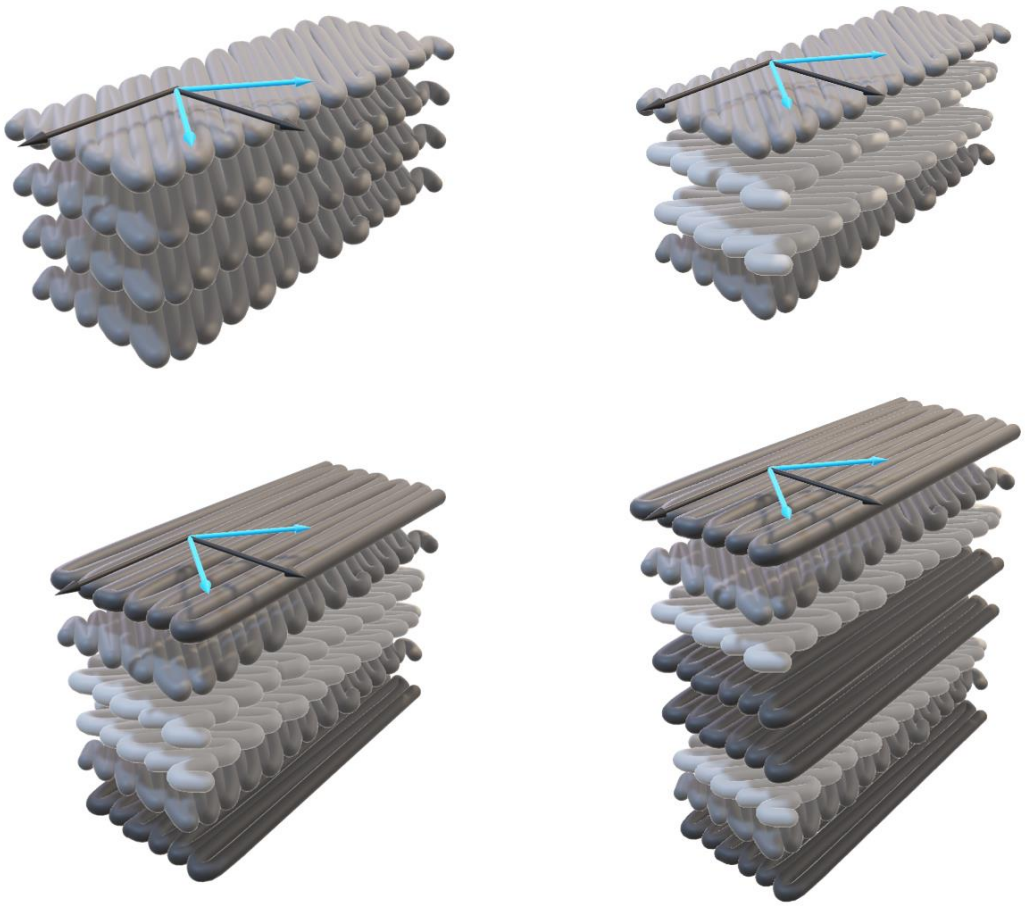

*Figure 13: Stacking sequences. Top: $[\theta]_4$, $[\pm\theta]_s$. Bottom: $[0,\pm\theta]_s$, $[0,\pm\theta,0]_s$*

## 3.4 FAILURE CHARACTERIZATION

### 3.4.1 FAILURE CRITERION

The failure criterion proposed was developed by Osswald and Osswald [35]. It is based on the method described by Gol'denblat and Kopnov [36] and improved to overcome some of its limitations.

The original criterion describes a scalar function that depends on the strength tensors and the stress state.

$$f = \left(F_{ij}\sigma_{ij}\right)^{\alpha} + \left(F_{ijkl}\sigma_{ij}\sigma_{kl}\right)^{\beta} + \left(F_{ijklmn}\sigma_{ij}\sigma_{kl}\sigma_{mn}\right)^{\gamma} \dots$$

The function was limited to include the second and fourth order tensors. The parameters α and β were assigned the values of 1 and $\frac{1}{2}$ respectively in order to maintain a linear scalar relationship with the stresses. Failure is expected for stress states with a value of $f$ greater than 1.

For a plane stress scenario, the criterion is reduced to:

$$\begin{aligned} f = {} & F_{11}\sigma_{11} + F_{22}\sigma_{22} + F_{12}\tau_{12} \\ & + (F_{1111}\sigma_{11}^2 + F_{2222}\sigma_{22}^2 + F_{1212}\tau_{12}^2 + 2F_{1122}\sigma_{11}\sigma_{22} + 2F_{1112}\sigma_{11}\tau_{12} \\ & + 2F_{2212}\sigma_{22}\tau_{12})^{\frac{1}{2}} \end{aligned}$$

Where the notation $\sigma_{ij}$ and $\tau_{ij}$ indicate axial and shear stresses as shown in Figure 14 and the terms $F_{ij}$, $F_{ijkl}$ represent the second and fourth order tensors that depend on engineering strength parameters.

These tensorial components can be obtained through mechanical tests. The independent parameters for the stress terms can be calculated from uniaxial tests under tensile and compressive loads. The shear terms similarly with pure torsion tests and the calculation of the interactive parameters requires combined loads.

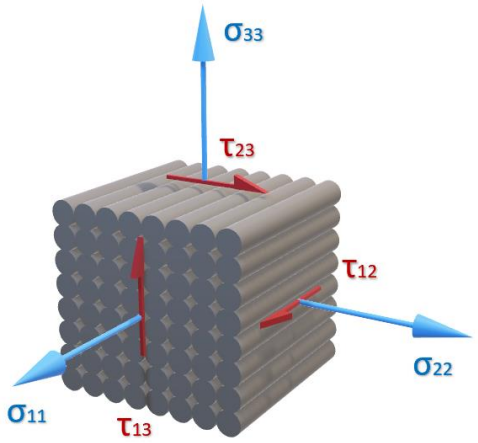


*Figure 14: Stress components on a representative element*

Gol'denblat and Kopnov [36] indicated the calculation of the term $F_{1122}$ for the interaction between $\sigma_{11} - \sigma_{22}$ with additional torsion tests of specimens with beads oriented in a 45º angle. They considered the interaction of the shear and the stresses to be negligible, assigning 0 for the values of $F_{1112}$ and $F_{22212}$.

This assumption was addressed by Osswald and Osswald [35]. They overcame this limitation by the calculation of the interactive terms with the use of the derivative of the failure surface within an arbitrary $\sigma_{ij} - \sigma_{kl}$ plane. The slope of the envelope in strategic locations can be computed by performing a series of combined loading mechanical tests around any point where the strength is known. The slopes are denoted $\lambda_k^{iijj}$ for those comprised in an axial stress plane or $\mu^{iiij}$ in a shear-axial plane. The subscript k in $\lambda_k^{iijj}$ denotes the four possible locations where the slope can be obtained. The interaction stress components are presented in Table 4 and a schematic of the slope at the $\sigma_{22}$-$\tau_{12}$ plane used to compute $F_{2212}$ term is shown in Figure 15.

*Table 4: Interaction stress components*

| Tensor component | Formula |
|---|---|
| $F_{iiij}$ | $\frac{F_{ii}}{\tau_{ij}^{u}} - F_{ijij}\mu^{iiij}$ |
| $F_{iijj}$ ($\lambda_1^{iijj}$) | $-\frac{\left(F_{ii} + F_{jj}\lambda_1^{iijj}\right)F_{iiii}^{1/2} + F_{iiii}}{\lambda_1^{iijj}}$ |
| $F_{iijj}$ ($\lambda_2^{iijj}$) | $-\left(F_{ii} + F_{jj}\lambda_2^{iijj}\right)F_{jjjj}^{1/2} - F_{jjjj}\lambda_2^{iijj}$ |
| $F_{iijj}$ ($\lambda_3^{iijj}$) | $\frac{\left(F_{ii} + F_{jj}\lambda_3^{iijj}\right)F_{iiii}^{1/2} - F_{iiii}}{\lambda_3^{iijj}}$ |
| $F_{iijj}$ ($\lambda_4^{iijj}$) | $\left(F_{ii} + F_{jj}\lambda_4^{iijj}\right)F_{jjjj}^{1/2} - F_{jjjj}\lambda_4^{iijj}$ |

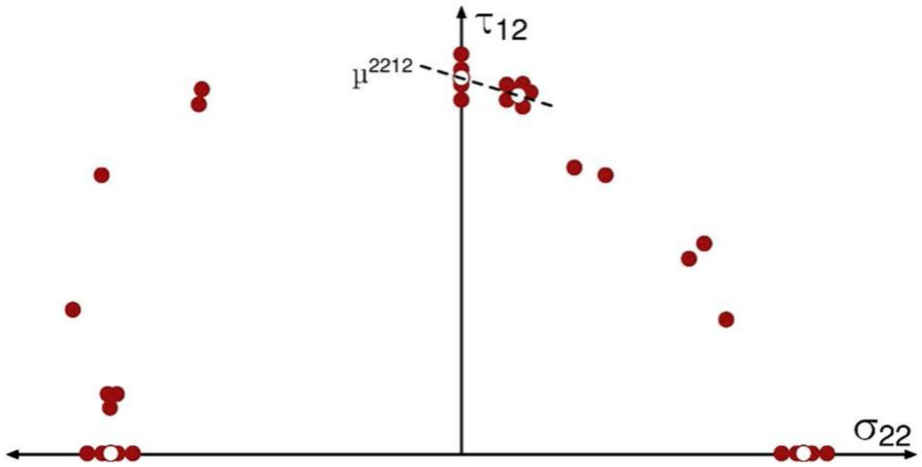


*Figure 15 Schematic of the slope in $\sigma_{22}$-$\tau_{12}$ plane [28]*

The calculation of the tensorial components are presented in Table 5, where $X_t$, $X_c$ are the tensile and compressive strengths in the first direction; $Y_t$ $Y_c$ in the second direction and S is the maximum shear strength.

*Table 5: Tensorial components*

| Component | Formula |
|---|---|
| $F_{11}$ | $\frac{1}{2}\left(\frac{1}{X_t}-\frac{1}{X_c}\right)$ |
| $F_{1111}$ | $\frac{1}{4}\left(\frac{1}{X_t}+\frac{1}{X_c}\right)^2$ |
| $F_{22}$ | $\frac{1}{2}\left(\frac{1}{Y_t}-\frac{1}{Y_c}\right)$ |
| $F_{2222}$ | $\frac{1}{4}\left(\frac{1}{Y_t}+\frac{1}{Y_c}\right)^2$ |
| $F_{12}$ | $0$ |
| $F_{1212}$ | $\frac{1}{S^2}$ |
| $F_{1122}$ (Gol'denblat-Kopnov) | $\frac{1}{8}\left[\left(\frac{1}{X_t}+\frac{1}{X_c}\right)^2+\left(\frac{1}{Y_t}+\frac{1}{Y_c}\right)^2-\left(\frac{1}{S_{45p}}+\frac{1}{S_{45n}}\right)^2\right]$ |
| $F_{1112}$ | $\frac{F_{11}}{S}-F_{1212}\mu^{1112}$ |
| $F_{2212}$ | $\frac{F_{22}}{S}-F_{1212}\mu^{2212}$ |

A standard method to determine the interactive term between the stresses has not been established. Different tests have been proposed to measure it, yet the results are not consistent. A biaxial stress state is needed for its calculation, but the ratio of the stresses when performing the tests was proven to be a great source for error. A small variance in one of the stresses greatly impacts the interactive term.[37]

The value for this coefficient $F_{1122}$ is bounded by the stability condition since the failure function must define a closed surface. Otherwise it would mean that for certain combined stress states the part would never fail.

In the axial stress plane $\tau_{12}$ is zero so the function takes the form

$$f = F_{11}\sigma_{11} + F_{22}\sigma_{22} + (F_{1111}\sigma_{11}^2 + F_{2222}\sigma_{22}^2 + 2F_{1122}\sigma_{11}\sigma_{22})^{\frac{1}{2}}$$

To define a closed surface the function $f$ must be continuous.

$$F_{1111}\sigma_{11}^2 + F_{2222}\sigma_{22}^2 + 2F_{1122}\sigma_{11}\sigma_{22} \geq 0$$

This equation can be rewritten as:

$$F_{1111}\sigma_{11}^2 + F_{2222}\sigma_{22}^2 + 2\sqrt{F_{1111}F_{2222}}\sigma_{11}\sigma_{22} - 2\sqrt{F_{1111}F_{2222}}\sigma_{11}\sigma_{22} + 2F_{1122}\sigma_{11}\sigma_{22} \geq 0$$

where the two additional terms cancel each other.

Rearranging the terms

$$\left(\sqrt{F_{1111}}\sigma_{11} + \sqrt{F_{2222}}\sigma_{22}\right)^2 - 2\sqrt{F_{1111}F_{2222}}\sigma_{11}\sigma_{22} + 2F_{1122}\sigma_{11}\sigma_{22} \geq 0$$

Or

$$\left(\sqrt{F_{1111}}\sigma_{11} - \sqrt{F_{2222}}\sigma_{22}\right)^2 + 2\sqrt{F_{1111}F_{2222}}\sigma_{11}\sigma_{22} + 2F_{1122}\sigma_{11}\sigma_{22} \geq 0$$

The first term is always greater than zero, the condition is fulfilled if

$$2F_{1122} \pm 2\sqrt{F_{1111}F_{2222}} \geq 0$$

This limits the value of $F_{1122}$.

$$-\sqrt{F_{1111}F_{2222}} \leq F_{1122} \leq \sqrt{F_{1111}F_{2222}}$$

### 3.4.2 MATERIAL AND TESTING

The material used for the failure surface characterization is carbon fiber reinforced nylon PA6. It can be used to build functional structures due to its high elastic modulus and the improved chemical and thermal resistance. It is easy to print and it has an excellent surface finish.[38] The content of short carbon fibers is 30 wt.% with an average length of 50-60 μm.

The recommended printing temperature is between 240-270ºC with a bed temperature of 80ºC to 100ºC. The layer height should not be lower than 0.25 mm since this may create too much back pressure in the hot end. The literature has proven the mechanical properties of the printed parts to be dependent on the processing parameters [21-23], therefore they should be kept constant for all the experiments. These recommended parameters are summarized in Table 6.

*Table 6: Recommended printing parameters*

| **Printing parameter** | **Value** |
|---|---|
| Nozzle temperature | 240-270 ºC |
| Bed temperature | 80-100 ºC |
| Layer height | > 0.25 mm |

The lack of standard methods to characterize AM materials require the design of custom specimen geometries to identify the tensorial components. Mazzei Capote

et al. [28] performed the characterization of the failure surface for printed ABS. The specimen geometries that were used in their research are shown in Figure 16.

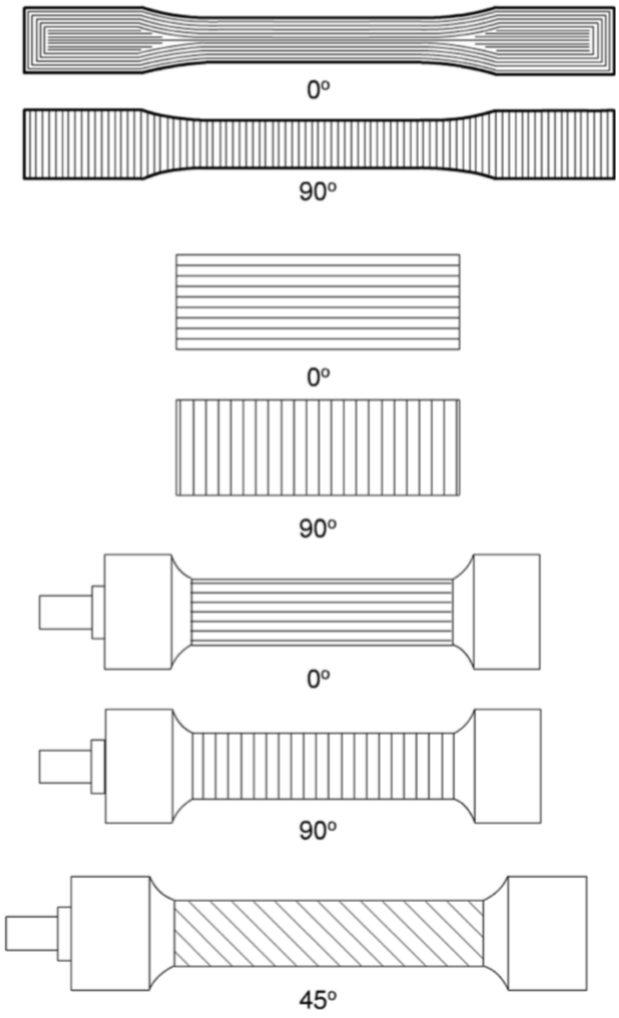


*Figure 16: Tensile, compressive and torsion specimens with respective bead orientation in the gauge section [28]*

In their experiments, the tensile samples followed the indications of ASTMD-638 Type I test. The tensile samples with 0º raster angle were used for the maximum strength in the first direction, $X_t$; and the ones with 90º raster angle were used for the maximum tensile strength in the second direction, $Y_t$.

The compressive samples were designed with a tubular cross section. If this experiment is done on solid samples the strengths would be higher because of hydrostatic stresses. The samples with 0º and 90 oriented beads were used to test the compressive strength in the first and second direction, respectively.

For the torsion specimens, they designed samples based on the EN ISO 3167, Type A specimens. Their cross-sectional area in the gauge section was the same as the one of the compressive samples and their ends were enlarged with three planes to enable a firm grip with the torsion test machine. The samples with a 45º raster angle were used to determine the ultimate positive and negative shear strength, $S_{45}^{p}$ and $S_{45}^{n}$. The samples with 0º and 90º were used for pure shear strength determination and the combined loading testing.

The strength and the elastic modulus in the first direction for CF-Nylon are 100 MPa and 7 GPa, respectively [39]. The rest of the material engineering parameters were estimated. In short fiber composites, transverse properties are matrix dominated [40], the maximum strength has been approximated by the strength of nylon PA6, 60 MPa . The tensile and compressive strengths in the principal directions are estimated to be of the same magnitude. However, compressive strengths are likely to be greater. Any defect in the material, under a tensile stress, acts as a stress concentrator.

The estimated parameters that are used for the failure surface are presented in Table 7.

*Table 7: Estimated strength parameters for CF nylon*

| Parameter | Estimated value |
|---|---|
| $X_t$ | 100 MPa |
| $X_c$ | -100 MPa |
| $Y_t$ | 60 MPa |
| $Y_c$ | -60 MPa |
| $S$ | 40 MPa |
| $S_{45}^{p}$ | 60 MPa |
| $S_{45}^{n}$ | 40 MPa |

# Chapter 4. ANALYSIS OF RESULTS

## 4.1 CLT ANALYSIS

### 4.1.1 UNIAXIAL LOAD

Different stacking sequences are studied under a tensile load aligned with the x axis. For all the cases presented in this section [NM]=[1,0,0,0,0,0]' MPa. In the following figures, the load divided by the height is plotted against the raster angle.

The first laminate that is studied consists of four unidirectional plies, shown in Figure 17. For this case, $\sigma_x$ is uniform in all the layers and therefore there is no progressive failure. The first and the last ply fail under the same load. As $\sigma_x$ is independent from the height $\frac{N_x}{h} = \sigma_x$, the load over the height is the stress in each layer so the failure with 0º and 90º raster angle are $X_t$ and $Y_t$ respectively.

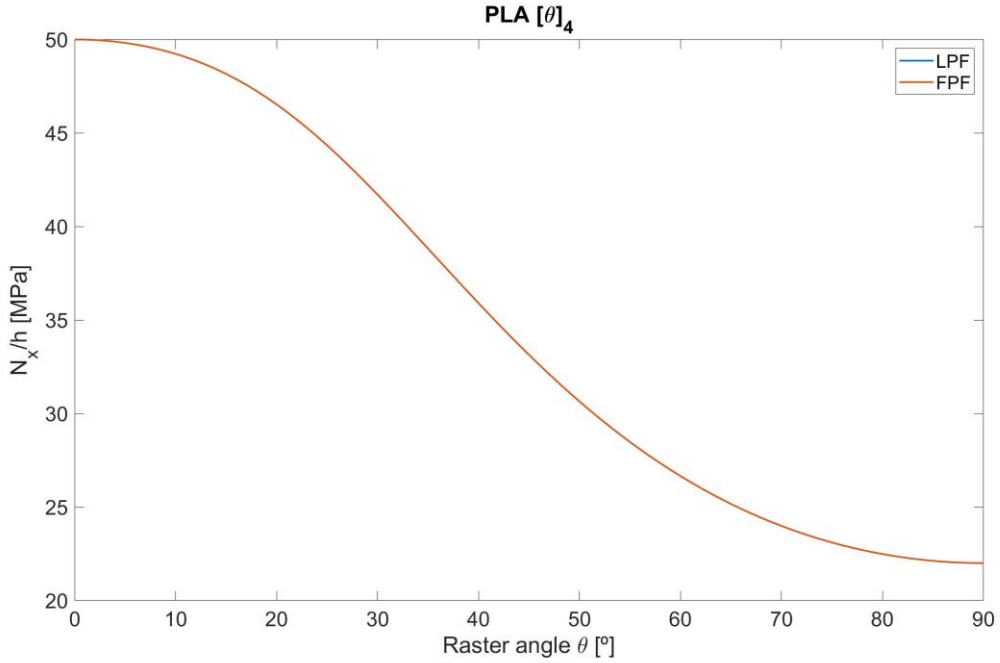


*Figure 17: PLA $[\theta]_4$ maximum load over height vs raster angle*

The strongest part is achieved with 0º raster angle for all the cases of this section, as this angle aligns the filaments with the load.

The next laminate studied is symmetric and balanced, its stacking sequence is $[0,\pm\theta]_s$. As it can be seen in Figure 18 for this stacking sequence the first ply does no longer fail at the same load as the last ply. This only happens when all the layers are aligned with a raster angle of 0º, which is the same as the previous unidirectional laminate. The value of $\frac{N_x}{h}$ is therefore the same as the previous case. As soon the plies are no longer perfectly aligned the last ply failure load drops significantly. This is due to the failure of the laminates with ±θ raster angle. These layers are discounted and now only two plies are left to hold the load. If the last ply failure yields lower loads, the failure of the parts is sudden. Once the first ply fails, the whole part fails.

For small values of θ the load breaks the filaments due to the stress in the first direction, they fail in fiber failure mode. As the raster angle increases, the stress in the second direction of the failed layers increases. Although they failed in fiber mode, they can still contribute to hold the load with the stress induced in their transverse direction. This trend is observed until the failure mode changes to shear or interfiber failure, where the failed filaments can hold load in their longitudinal direction but no longer in the transverse direction. After this discontinuity, the LPF load decreases until a local minimum is reached and slightly increases afterwards.

The addition of two layers aligned with the external load does not increase the load required to break the first ply. Since the elastic modulus in the first and the second direction is very similar, the deformation of the laminate will be same as the previous case, and the load required to break the weaker layers is the same.

This same stacking sequence was analyzed for E-glass/Epoxy composite and the results are shown in Figure 19 for comparison. The difference in the elastic modulus and the strengths of the principal directions is more significant for composite

materials and the effects of this difference can be seen in the laminate behavior. For small values of θ, the slope of the last ply failure line has a small positive value. The transverse elastic modulus is very small compared to the longitudinal modulus, so once the fibers fail, the matrix contribution to hold the load is smaller than in the case for PLA. In this case, once the failure is no longer due to the fibers, the last ply failure increases and for values of θ greater than 45º it is greater than the first ply failure load. When the first layers fail, their contribution of the load is redistributed in the remaining layers. In this case, they can still hold the load of the discounted plies as they are both stiffer and stronger. For composite materials, the last ply fails at a higher load, the failure is progressive, when the first ply fails the failure is not sudden. In this case, regarding the first ply failure when the raster angle is close to 90º, the addition of two layers with 0º raster angle increases the load that is required to break the weakest layers. While a unidirectional laminate would fail at 39 MPa, this laminate breaks at 70 MPa. The new plies contribute to the stiffness of the laminate in the x direction with their longitudinal elastic modulus, increasing the global value of the stiffness in this direction for the laminate.

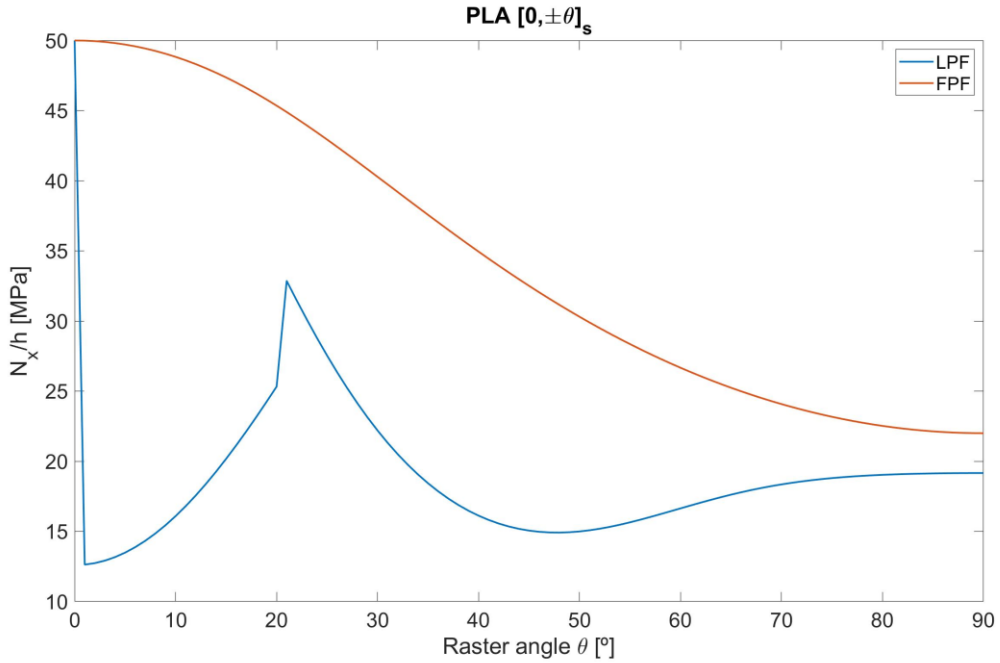


*Figure 18: PLA [0, ±θ]$_s$ maximum load over height vs raster angle*

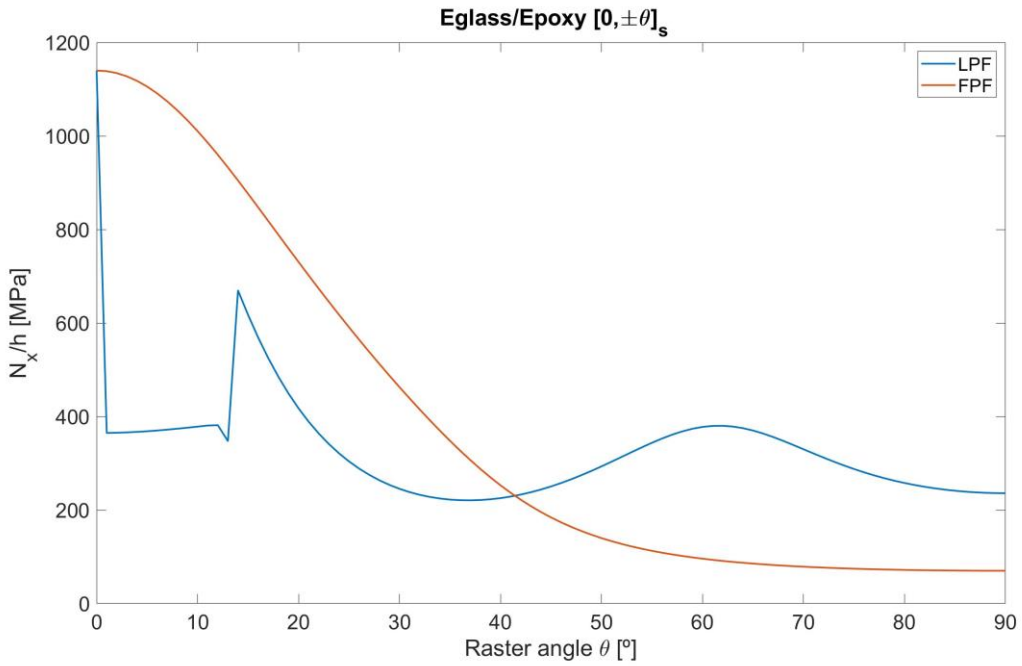


*Figure 19: E-glass/ Epoxy [0, ±θ]s maximum load over height vs raster angle*

For the last laminate of this section, two more 0º raster angle layers were added. The stacking sequence is still symmetric and balanced and there is the same number of layers aligned with the load as the number of layers that vary their raster angle. For the FFF printed part, at high values of the raster angle, progressive failure is expected. There are more layers whose strongest direction is aligned with the external load than in the previous case. The stacking sequence is [0, ±θ,0]s.

The results for PLA are presented in Figure 20: PLA [0, ±θ,0]s maximum load over height vs raster angleFigure 20 and for E-glass/Epoxy in Figure 21. For both materials, the last ply failure line is shifted upwards compared to the previous case. Their shape has not changed as the same interactions occur between the failed layers and the remaining layers.

In this case for PLA the last ply failure load is greater than the one required for the first ply failure. The x direction of the laminate is reinforced with the additional layers. Although the strength in the first direction is more than twice the strength in the second direction, one layer was not able to hold the load of the two failed ones. The ratio between failed layers and aligned layers must be greater than 2.

For E-glass/ Epoxy, as a result of shifting the line, the last ply failure load is greater than the first ply failure for values of θ greater than 35º. For this material, the elastic modulus of the aligned layers increases the stiffness in the x direction of the laminate, so the first ply failure line is also shifted. There is progressive failure in a wider range of values for the raster angle.

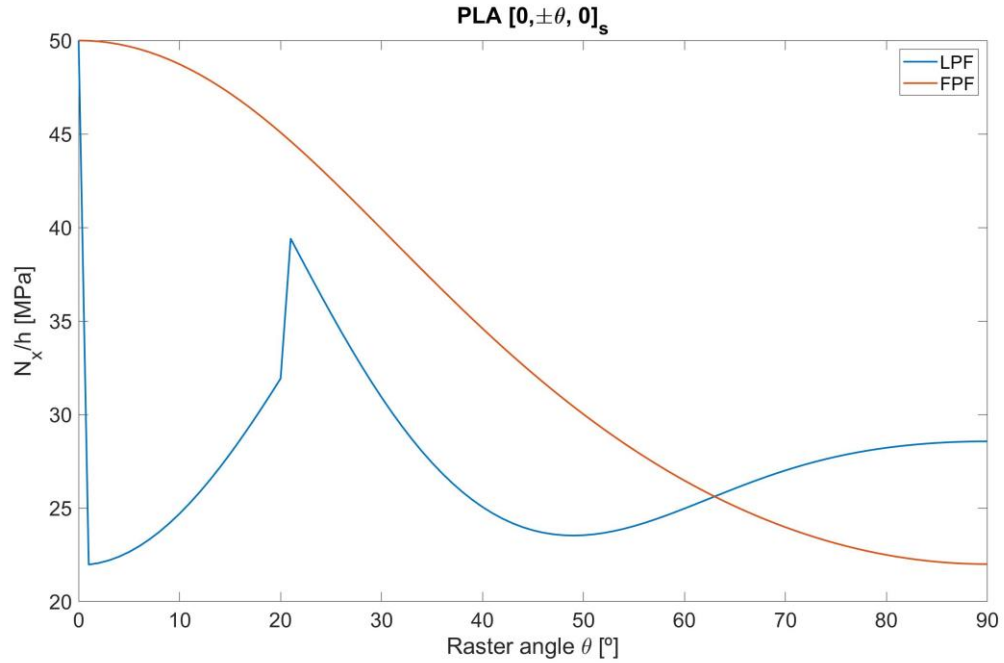


*Figure 20: PLA [0, ±θ,0]s maximum load over height vs raster angle*

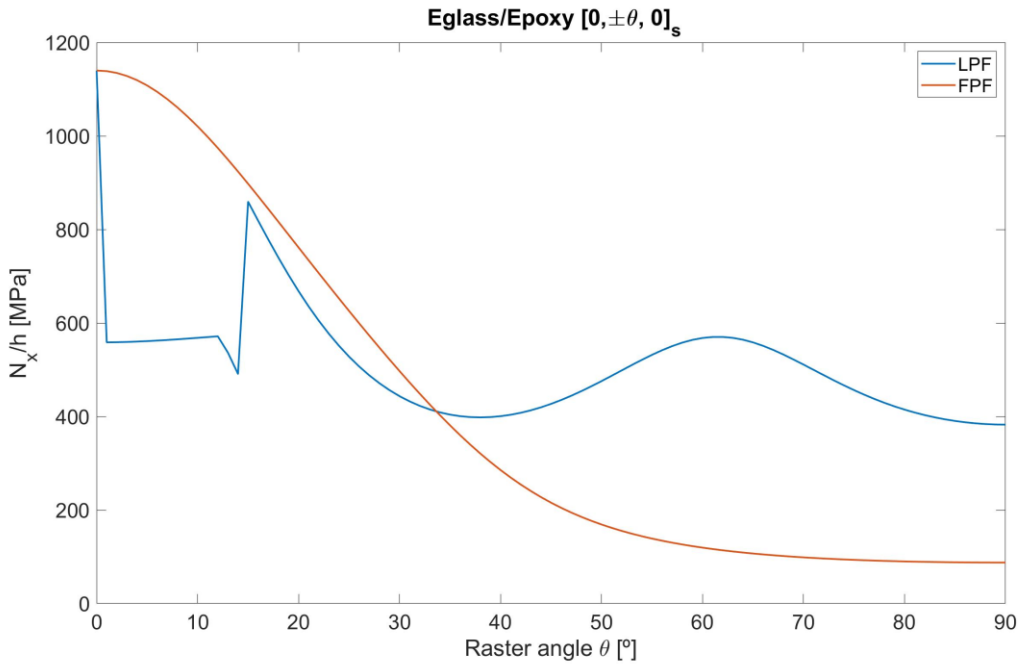


*Figure 21: E-glass/ Epoxy [0, ±θ,0]s maximum load over height vs raster angle*

### 4.1.2 BIAXIAL LOAD

For this section, the laminates are subject to a biaxial load. The resultant force in the x direction is five times greater than the force in the y direction. The value of the vector NM is [1,0.2,0,0,0,0]'. In this section the figures plot the maximum load N over the height ( $\frac{N}{h}$);  this means $N_x$=N and $N_y$=$\frac{N}{5}$. The stacking sequence that is studied is a symmetric and balanced laminate with four layers, [ ±θ]s.

For the printed material, shown in  Figure 22, the stiffness of the laminate does not depend on the direction of the raster angle. The strongest part is achieved aligning the filaments with the dominant component of the load. Moreover, the interaction of the forces has a strengthening effect on the laminate, now the maximum load is greater than 50 MPa for a raster angle of 0º.

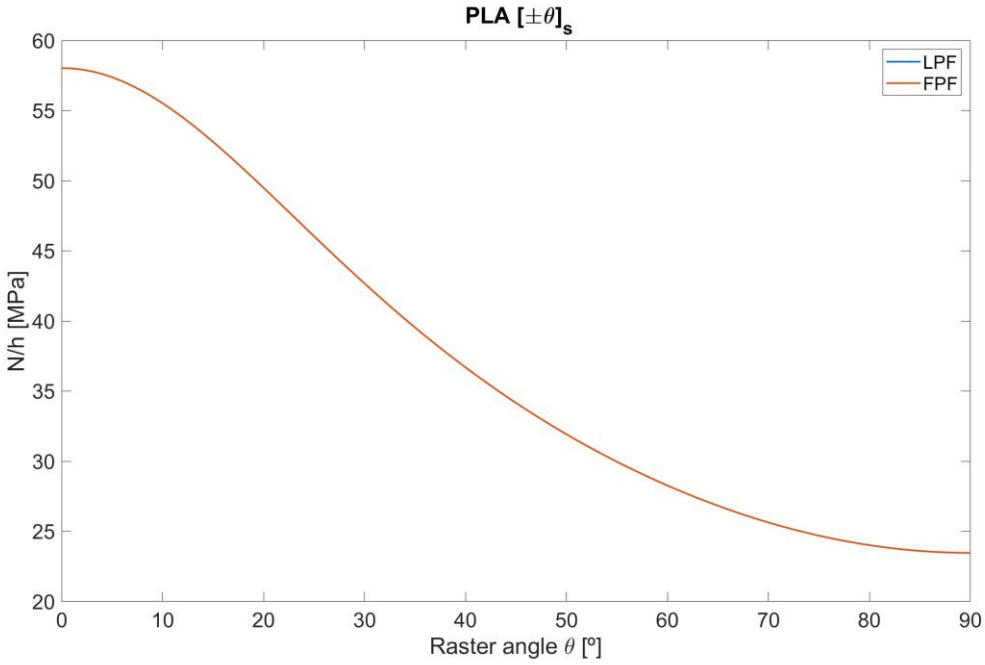


*Figure 22: PLA [ ±θ]s under biaxial load*

The stiffness of the composite is direction dependent as previously mentioned and the strength is also highly anisotropic. The maximum load for E-glass/ Epoxy subject to the biaxial stress is shown in Figure 23.

When all the fibers are aligned in the x direction, the transverse force is causing the matrix failure. Although the $N_y$ is five times smaller than $N_x$, the failure happens in the y direction because the matrix strength is smaller than the fiber strength. For this composite it is almost 30 times smaller. Varying the raster angle first increases the load carrying capacity of the laminate until a maximum is reached at 25º. This is the optimal raster angle for this stacking sequence. Aligning the fibers with the principal direction of the force gives best results.

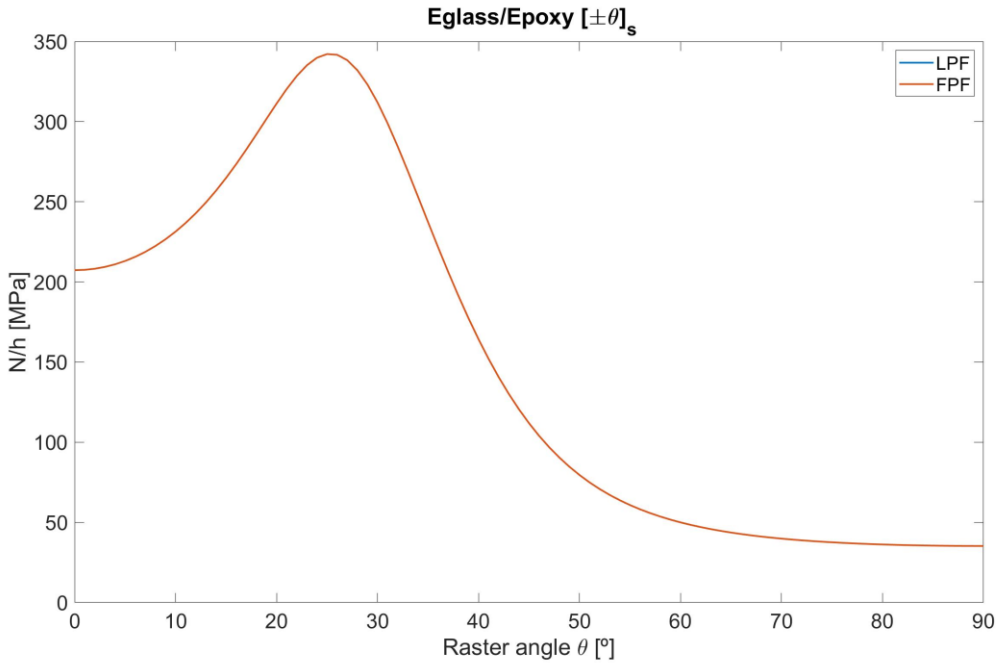


*Figure 23: E-glass/Epoxy [ ±θ]s under biaxial load*

The comparison done in this section has shown that the optimization for printed parts does not entail major improvements. The benefits of optimizing the raster angle obtained for the composite materials are due to the difference in the strengths and the elastic modulus in the first and second direction of the laminae. The

difference in the parameters in the composites is at least one order of magnitude, while for the printed parts, the elastic modulus is the same in all the directions and the strength is also not as anisotropic.

### 4.1.3 EFFECT OF YIELDING IN THE SECOND DIRECTION

A unidirectional laminate of PLA was subject to a tensile load to study the effect of yielding in the second direction on the mechanical behavior.

The result is shown in Figure 24. It can be observed that the load that is required to break the first ply is greater when the yielding is considered for raster angles close to 90º. However, this increase of the load is not significant and only occurs for a small range of raster angles. This effect was considered negligible.

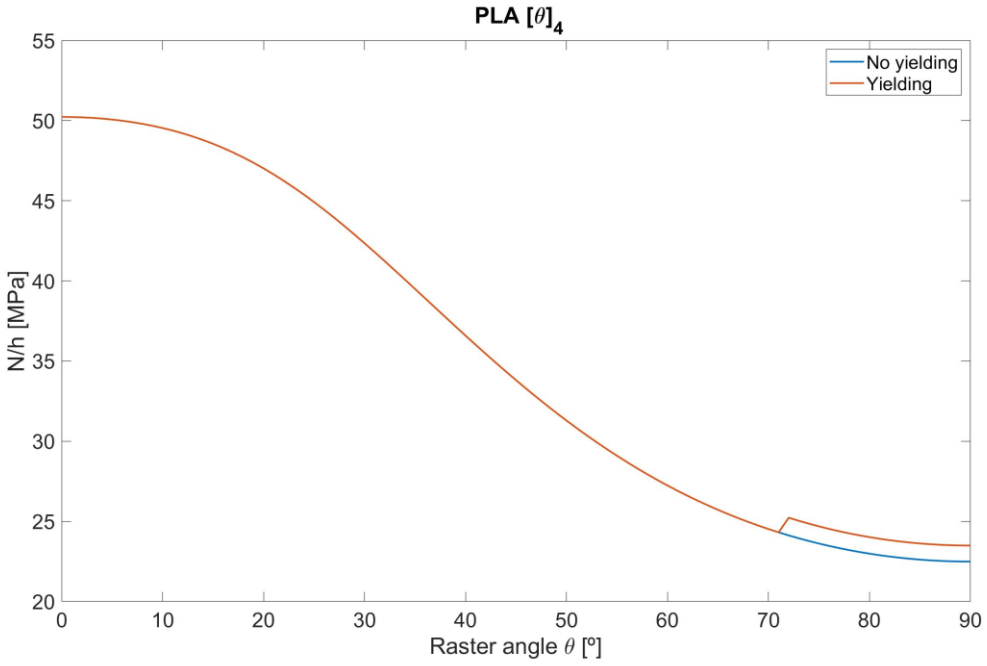


*Figure 24: Comparison of PLA [ ±θ]₄ with and without accounting for the yielding effect*

## 4.2 FAILURE SURFACE

The tensorial components were calculated with the formulas in Table 5, the numerical values are presented in Table 8.

*Table 8: Numerical values for the failure function coefficients*

| Component | Value |
|---|---|
| $F_{11}$ | 0 |
| $F_{1111}$ | $1.000*10^{-4}$ |
| $F_{22}$ | 0 |
| $F_{2222}$ | $2.778*10^{-4}$ |
| $F_{12}$ | 0 |
| $F_{1212}$ | $6.250*10^{-4}$ |
| $F_{1122}$ | $-2.813*10^{-4}$ |
| $F_{1112}$ | $6.250*10^{-5}$ |
| $F_{2212}$ | $6.250*10^{-5}$ |

The null values for $F_{11}$ and $F_{22}$ are due to the approximation of the tensile and compressive strengths to be equal. In reality, the compressive strength is likely to be higher than the tensile strength so these parameters would have a nonzero value.

The calculation of $F_{ii12}$ was done with an arbitrary $\mu^{ii12} = -0.1$, the effect of this slope will be discussed in section 4.2.2.

### 4.2.1 INTERACTION $\sigma_{11} - \sigma_{22}$

The failure function in the axial stresses plane describes an ellipse. The points where the $\sigma_{11}$ and $\sigma_{22}$ axes are intercepted are the strengths in the first and second direction, respectively. As it can be seen in Figure 25 all the curves coincide in these four points.

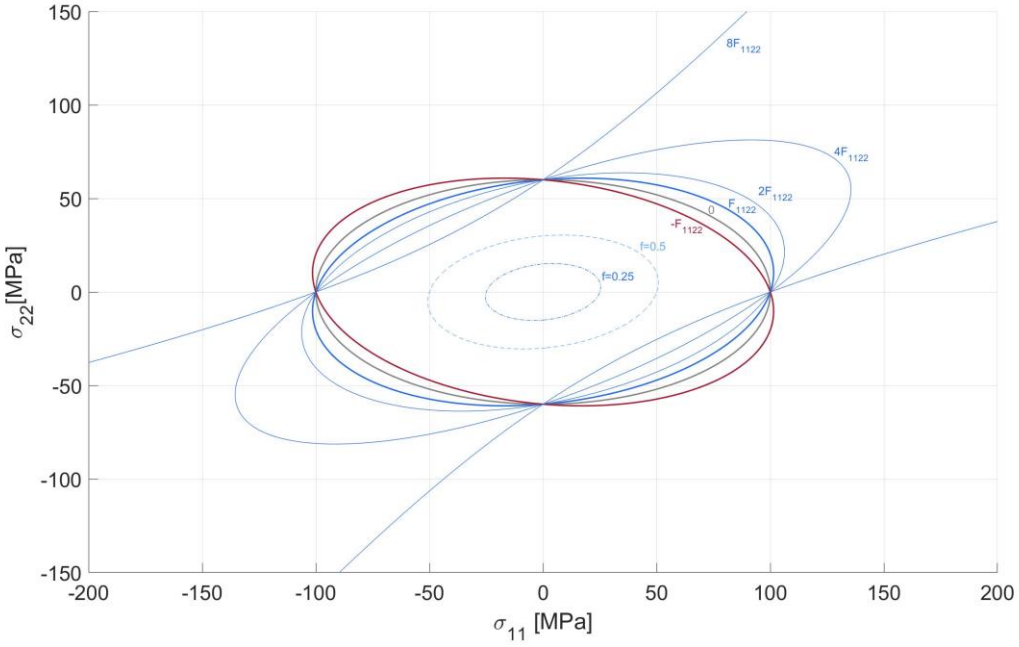


*Figure 25: Failure envelope in the axial stress plane $\sigma_{11}$-$\sigma_{22}$*

The value for the interactive parameter was varied for a sensitivity analysis. It was first calculated with the Gol'denblat-Kopnov formula, resulting in a negative value, $F_{1122}$=-2.813*10$^{-4}$. This enlarges the safety region in the first and third quadrant which captures the strengthening effect of a biaxial loading state when both $\sigma_{11}$ and $\sigma_{22}$ are either tensile or compressive. For materials with a positive Poisson's ratio this phenomenon is expected.

When a load is applied and the material deforms in one direction, the perpendicular direction will also deform with the ratio defined by the Poisson's modulus. If the deformation is constrained a stress is induced. When a material with a positive ratio

is subject to a biaxial load with both directions tensile or both compressive, the stress induced in the perpendicular direction counters the effect of the external load. The opposite effect occurs for auxetic materials [41], those with a negative Poisson's ratio. Their interactive parameter $F_{1122}$ is positive and the region enlarged is in the second and fourth quadrant. The shape of the failure envelope for these materials is more similar to the red curve in Figure 25.

As the absolute value of $F_{1122}$ increases the principle axes of the ellipse rotate about the perpendicular axis and the area enlarges. The value for the interactive parameter can increase until a limit is reached since it is bounded by the stability condition as explained in section 3.4.1. The curve shown in Figure 25 with 8 $F_{1122}$ is an example of an infeasible solution. It does not describe a closed surface.

### 4.2.2 INTERACTION $\sigma_{ii} - \tau_{12}$

The failure envelope for the shear and the axial stresses is very similar in both $\sigma_{11}$-$\tau_{12}$ and $\sigma_{22}$-$\tau_{12}$ planes. The function is shown in Figure 26 for $\sigma_{11}$-$\tau_{12}$ and in Figure 27 for $\sigma_{22}$-$\tau_{12}$. Without interaction the function describes an ellipse with the major axis in the $\sigma_{ii}$ axis. In the figures, the axes for $\sigma_{ii}$ and $\tau_{12}$ are not equally scaled.

A negative slope enlarges the region in the second quadrant, capturing a strengthening effect for shear and negative stresses. On the contrary, a positive slope means there is a strengthening effect for shear and positive stresses.

Similarly to the value for $F_{1122}$, some values for $\mu_{ii12}$ could make the curve describe a discontinuous function. However, since this parameter is fitted to experimental data, it is unlikely to happen.

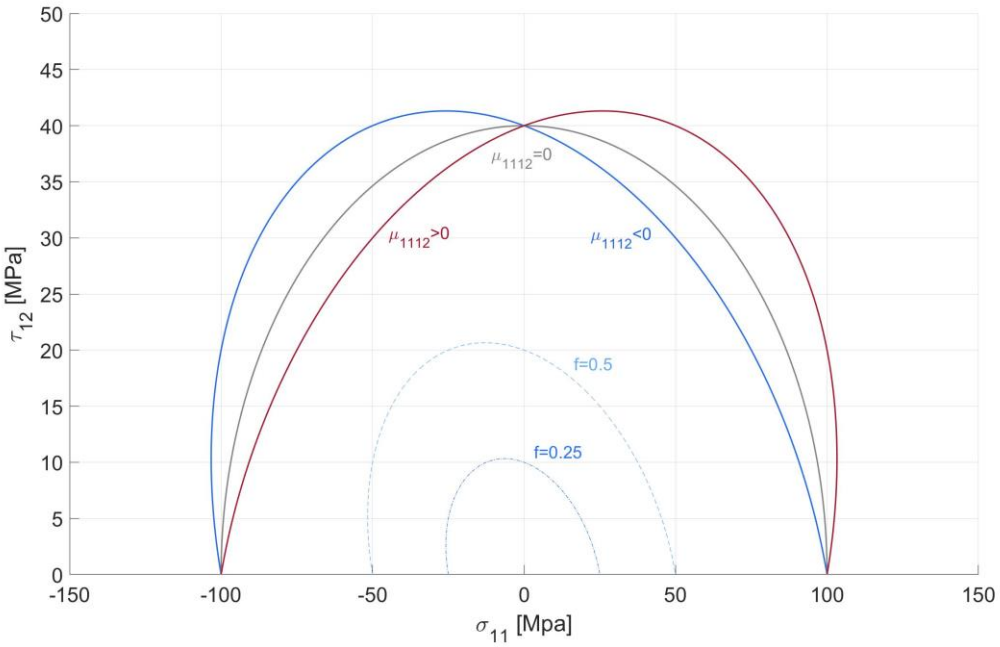


*Figure 26: Failure envelope in the shear axial stress plane $\sigma_{11}$-$\tau_{12}$*

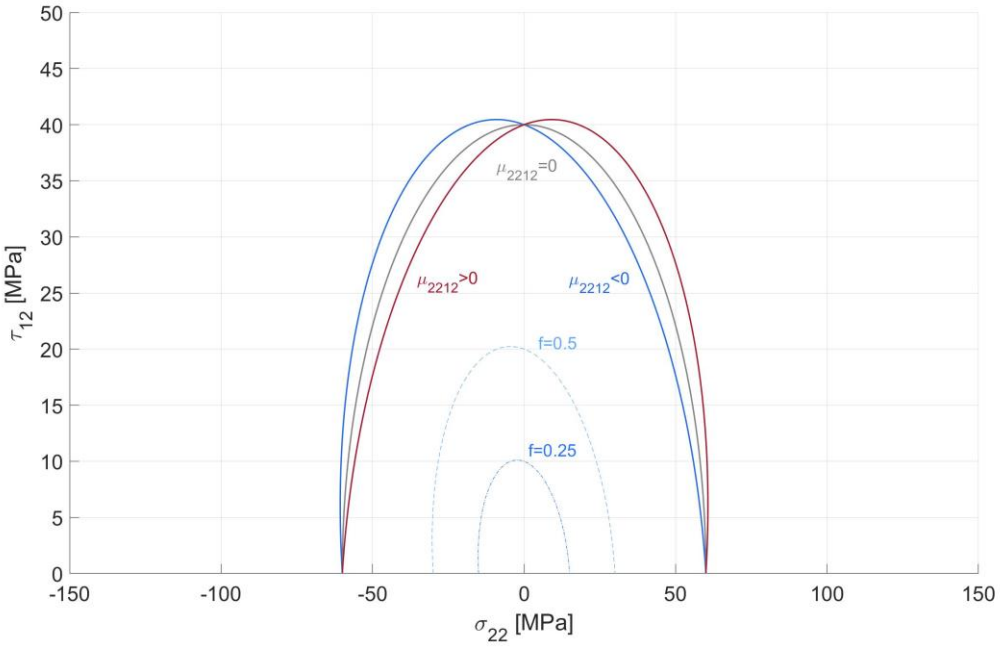


*Figure 27: Failure envelope in the shear axial stress plane $\sigma_{22}$-$\tau_{12}$*

### 4.2.3 3D FAILURE SURFACE

The failure function that is calculated with the numerical values in Table 8 is plotted in the $\sigma_{11}$-$\sigma_{22}$-$\tau_{12}$ space in Figure 28. It includes the values of $f = 1, 0.75, 0.5$ and $0.25$ representing the safety factors of 1, 4/3, 2 and 4 respectively for reference.

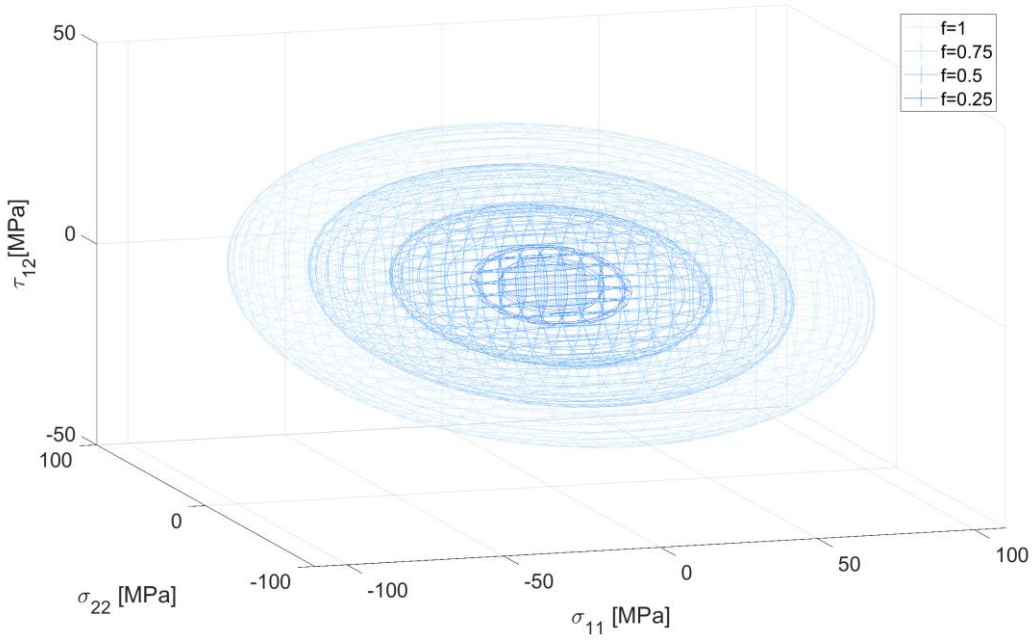


*Figure 28: 3D failure surface for CF nylon*

With experimental testing to characterize the material parameters, this failure criterion can be easily implemented to simulation software for failure determination.

# Chapter 5. CONCLUSIONS AND FUTURE WORK

## 5.1 CONCLUSIONS

FFF printed parts present a similar structure to laminated composites. The classical lamination theory has been proven to be a valid model to predict their mechanical performance. However, there are also some differences between continuous fibers composites and the FFF parts.

Both materials have anisotropic properties. For the case of composites the fiber direction is both stiffer and stronger, while for the case of printed parts this direction is only stronger. Since the elastic modulus is not direction dependent, the stresses will be evenly distributed in all the plies. The consequences of this difference on FFF multidirectional laminates are mainly:

- Once the weaker layers fail and their contribution of the load is redistributed the whole part fails. Progressive failure analysis is only observed when the remaining plies are able to hold the load and continue with their deformation. Because the strength in the first direction and the second direction are of the same magnitude these parts present sudden failure. For composites progressive failure is easier to achieve since the strength in the first direction is normally and order of magnitude superior to the strength in the second direction.
- There is no stiffening effect with the addition of fibers aligned in a certain direction. The first ply of the laminate will fail under the same load regardless of the addition of an aligned lamina.
- Under biaxial loads, the strongest parts are achieved by aligning the filaments to the highest component of the external force. If the transverse direction does not fail, a strengthening effect will be observed.

The effect of yielding in the second direction was also considered and neglected because the consequences of this phenomenon did not significantly change the behavior of the laminate.

Lastly, the failure criterion proposed by Osswald and Osswald [35] is capable of capturing all the interactions between the shear and axial stresses. With experimental tests to determine the tensorial components, the criterion can be easily implemented in simulation software.

## 5.2 RECOMMENDATIONS FOR FUTURE WORK

The methodology for the characterization of printed materials was explained but experimental tests are needed for the implementation of this work.

# Chapter 6. BIBLIOGRAPHY

1. Goncalves, J., et al., *Electrically Conductive Polyetheretherketone Nanocomposite Filaments: From Production to Fused Deposition Modeling.* Polymers (Basel), 2018. **10**(8).
2. Rinaldi, M., et al., *Additive layer manufacturing of poly (ether ether ketone) via FDM.* Composites Part B: Engineering, 2018. **145**: p. 162-172.
3. Gebisa, A.W., *Influence of 3D Printing FDM Proce.* 2019.
4. Wu, W., et al., *Influence of Layer Thickness and Raster Angle on the Mechanical Properties of 3D-Printed PEEK and a Comparative Mechanical Study between PEEK and ABS.* Materials (Basel), 2015. **8**(9): p. 5834-5846.
5. Wang, P., et al., *Effects of printing parameters of fused deposition modeling on mechanical properties, surface quality, and microstructure of PEEK.* Journal of Materials Processing Technology, 2019. **271**: p. 62-74.
6. Gebisa, A.W. and H.G. Lemu, *Investigating Effects of Fused-Deposition Modeling (FDM) Processing Parameters on Flexural Properties of ULTEM 9085 using Designed Experiment.* Materials (Basel), 2018. **11**(4).
7. Cicala, G., et al., *Engineering thermoplastics for additive manufacturing: a critical perspective with experimental evidence to support functional applications.* J Appl Biomater Funct Mater, 2017. **15**(1): p. 0.
8. Deng, X., et al., *Mechanical Properties Optimization of Poly-Ether-Ether-Ketone via Fused Deposition Modeling.* Materials (Basel), 2018. **11**(2).
9. Cuan-Urquizo, E., et al., *Characterization of the Mechanical Properties of FFF Structures and Materials: A Review on the Experimental, Computational and Theoretical Approaches.* Materials (Basel), 2019. **12**(6).
10. Molitch-Hou, M., *Overview of additive manufacturing process*, in *Additive Manufacturing*. 2018. p. 1-38.
11. Wiberg, A., *Towards Design Automation for Additive Manufacturing : A Multidisciplinary Optimization approach*. 2019.
12. Gibson, I., D. Rosen, and B. Stucker, *Additive Manufacturing Technologies*. 2010: Springer.
13. Editors, E.B. *3D printing*. 2020; Available from: https://www.britannica.com/technology/3D-printing.
14. Groover, M.P., *Fundamentals of Modern Manufacturing*. 5th ed.: Wiley.
15. CustomPartNet, *Laminated Object Manufacturing (LOM)*. 2008.
16. *Todos los Detalles Sobre la Tecnología de Impresión 3D FDM*. Available from: https://www.tridimx.com/blog/todos-los-detalles-sobre-la-tecnologia-de-impresion-3d-fdm/.
17. Daniel, I.M. and O. Ishai, *Engineering Mechanics of Composite Materials*. 2nd ed. 2006: Oxford University Press.

18. Rankouhi, B., et al., *Failure Analysis and Mechanical Characterization of 3D Printed ABS With Respect to Layer Thickness and Orientation.* Journal of Failure Analysis and Prevention, 2016. **16**(3): p. 467-481.
19. Chacón, J.M., et al., *Additive manufacturing of PLA structures using fused deposition modelling: Effect of process parameters on mechanical properties and their optimal selection.* Materials & Design, 2017. **124**: p. 143-157.
20. Rajpurohit, S. and H. Dave, *Analysis of tensile strength of a fused filament fabricated PLA part using an open-source 3D printer*. The International Journal of Advanced Manufacturing Technology, 2019. **101**.
21. Ning, F., et al., *Additive manufacturing of carbon fiber-reinforced plastic composites using fused deposition modeling: Effects of process parameters on tensile properties.* Journal of Composite Materials, 2016. **28**.
22. Justo, J., et al., *Characterization of 3D printed long fibre reinforced composites.* Composite Structures, 2018. **185**: p. 537-548.
23. Tekinalp, H.L., et al., *Highly oriented carbon fiber–polymer composites via additive manufacturing.* Composites Science and Technology, 2014. **105**: p. 144-150.
24. Li, L., et al., *Composite Modeling and Analysis for Fabrication of FDM Prototypes with Locally Controlled Properties.* Journal of Manufacturing Processes, 2002. **4**(2): p. 129-141.
25. Casavola, C., et al., *Orthotropic mechanical properties of fused deposition modelling parts described by classical laminate theory.* Materials & Design, 2016. **90**: p. 453-458.
26. Somireddy, M., C.V. Singh, and A. Czekanski, *Analysis of the Material Behavior of 3D Printed Laminates Via FFF*. Experimental Mechanics, 2019. **59**(6): p. 871-881.
27. Alaimo, G., et al., *Influence of meso-structure and chemical composition on FDM 3D-printed parts.* Composites Part B: Engineering, 2017. **113**: p. 371-380.
28. Mazzei Capote, G.A., et al., *Failure surface development for ABS fused filament fabrication parts.* Additive Manufacturing, 2019. **28**: p. 169-175.
29. Mazzei Capote, G.A., A. Redmann, and T.A. Osswald, *Validating a Failure Surface Developed for ABS Fused Filament Fabrication Parts through Complex Loading Experiments.* Journal of Composites Science, 2019. **3**(2).
30. Yao, T., et al., *A novel generalized stress invariant-based strength model for inter-layer failure of FFF 3D printing PLA material.* Materials & Design, 2020. **193**.
31. Croccolo, D., M. De Agostinis, and G. Olmi, *Experimental characterization and analytical modelling of the mechanical behaviour of fused deposition processed parts made of ABS-M30.* Computational Materials Science, 2013. **79**: p. 506-518.
32. Cuan-Urquizo, E. and A. Bhaskar, *Flexural elasticity of woodpile lattice beams.* European Journal of Mechanics - A/Solids, 2018. **67**: p. 187-199.
33. Rodrı´guez, J.F., J.P. Thomas, and J.E. Renaud, *Design of Fused-Deposition ABS Components for Stiffness and Strength.* Journal of Mechanical Design, 2003. **125**(3): p. 545-551.
34. Y. Song, Y.L., W.Song, K. Yee, V.L. Tagarelli, *Measurements of the mechanical response of unidirectional 3D-printed PLA.* Materials & Design, 2017.
35. Osswald, P.V. and T.A. Osswald, *A strength tensor based failure criterion with stress interactions.* Polymer Composites, 2018. **39**(8): p. 2826-2834.

36. Gol'denblat, I.I. and V.A. Kopnov, *Strength of glass-reinforced plastics in the complex stress state.* Polymer Mechanics, 1965. **1**(2): p. 54-59.
37. Christian, H.W., *The significance and measurement of the Tsai-Wu normal interaction parameter*. 1993, Oregon State
38. *3DXTech*. Available from: https://www.3dxtech.com/carbon-fiber-filaments/carbonx-nylon-pa6-cf/.
39. *Polymaker*. Available from: https://cdn-3d.niceshops.com/upload/file/PolyMide_PA6-CF_TDS_EN_V4.pdf.
40. Fu, S.-y., B. Lauke, and Y.-w. Mai, *Strength of short fibre-reinforced polymers*, in *Science and Engineering of Short Fibre-Reinforced Polymer Composites*. 2019. p. 91-137.
41. Lakes, R.S., *Negative-Poisson's-Ratio Materials: Auxetic Solids.* Annual Review of Materials Research, 2017. **47**(1): p. 63-81.

# ANNEX I

## *CLASSICAL LAMINATION THEORY*

The elastic behavior of multi layered materials can be calculated using the classical lamination theory. For orthotropic materials nine independent elastic constants are needed to characterize the mechanical response.

- $E_1$ $E_2$ $E_3$ = Young's moduli along the principal directions
- $G_{12}$ $G_{23}$ $G_{13}$ = shear moduli in 1-2,2-3, and 1-3 planes, respectively
- $\nu_{12}$ $\nu_{23}$ $\nu_{13}$ = Poisson's ratios

The general equations can be simplified for orthotropic materials, the stress-strain relations are:

$$\begin{bmatrix}\sigma_1\\ \sigma_2\\ \sigma_3\\ \tau_4\\ \tau_5\\ \tau_6\end{bmatrix} = \begin{bmatrix}C_{11} & C_{12} & C_{13} & 0 & 0 & 0\\ C_{12} & C_{22} & C_{23} & 0 & 0 & 0\\ C_{13} & C_{23} & C_{33} & 0 & 0 & 0\\ 0 & 0 & 0 & C_{44} & 0 & 0\\ 0 & 0 & 0 & 0 & C_{55} & 0\\ 0 & 0 & 0 & 0 & 0 & C_{66}\end{bmatrix}\begin{bmatrix}\varepsilon_1\\ \varepsilon_2\\ \varepsilon_3\\ \gamma_4\\ \gamma_5\\ \gamma_6\end{bmatrix}$$

$$\begin{bmatrix}\varepsilon_1\\ \varepsilon_2\\ \varepsilon_3\\ \gamma_4\\ \gamma_5\\ \gamma_6\end{bmatrix} = \begin{bmatrix}S_{11} & S_{12} & S_{13} & 0 & 0 & 0\\ S_{12} & S_{22} & S_{23} & 0 & 0 & 0\\ S_{13} & S_{23} & S_{33} & 0 & 0 & 0\\ 0 & 0 & 0 & S_{44} & 0 & 0\\ 0 & 0 & 0 & 0 & S_{55} & 0\\ 0 & 0 & 0 & 0 & 0 & S_{66}\end{bmatrix}\begin{bmatrix}\sigma_1\\ \sigma_2\\ \sigma_3\\ \tau_4\\ \tau_5\\ \tau_6\end{bmatrix}$$

In compact notation:

$[\sigma] = [C][\varepsilon] \quad [\varepsilon] = [S][\sigma]$

Where [C] is the stiffness matrix and [S] is the compliance matrix, which are calculated from the material constants.

In this investigation only two-dimensional stress states are studied. There are no out of plane or surface loads. This is known as a plane stress scenario. For these cases, reduced matrices can be used to simplify the calculations.

$$\begin{bmatrix}\varepsilon_1\\ \varepsilon_2\\ \gamma_{12}\end{bmatrix}=\begin{bmatrix}S_{11} & S_{12} & 0\\ S_{12} & S_{22} & 0\\ 0 & 0 & S_{55}\end{bmatrix}\begin{bmatrix}\sigma_1\\ \sigma_2\\ \tau_{12}\end{bmatrix}\quad \begin{bmatrix}\sigma_1\\ \sigma_2\\ \tau_{12}\end{bmatrix}=\begin{bmatrix}Q_{11} & Q_{12} & 0\\ Q_{12} & Q_{22} & 0\\ 0 & 0 & Q_{55}\end{bmatrix}\begin{bmatrix}\varepsilon_1\\ \varepsilon_2\\ \gamma_{12}\end{bmatrix}$$

In terms of engineering constants:

$$\begin{bmatrix}\varepsilon_1\\ \varepsilon_2\\ \gamma_{12}\end{bmatrix}=\begin{bmatrix}\frac{1}{E_1} & \frac{-\nu_{12}}{E_1} & 0\\ \frac{-\nu_{12}}{E_1} & \frac{1}{E_2} & 0\\ 0 & 0 & \frac{1}{G_{12}}\end{bmatrix}\begin{bmatrix}\sigma_1\\ \sigma_2\\ \tau_{12}\end{bmatrix}\quad \begin{bmatrix}\sigma_1\\ \sigma_2\\ \tau_{12}\end{bmatrix}=\begin{bmatrix}\frac{E_1}{1-\nu_{12}*\nu_{21}} & \frac{\nu_{21}*E_1}{1-\nu_{12}*\nu_{21}} & 0\\ \frac{\nu_{21}*E_1}{1-\nu_{12}*\nu_{21}} & \frac{E_2}{1-\nu_{12}*\nu_{21}} & 0\\ 0 & 0 & G_{12}\end{bmatrix}\begin{bmatrix}\varepsilon_1\\ \varepsilon_2\\ \gamma_{12}\end{bmatrix}$$

It can be noted that the number of independent material constants is now reduced to only four: $E_1$, $E_2$, $G_{12}$ and $\nu_{12}$.

These equations describe stresses and strains in local axes but can also be transformed to global axes. The relationship is defined by the transformation matrix:

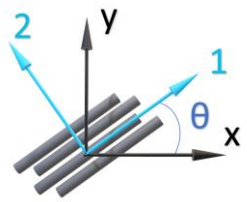


$$[T]=\begin{bmatrix}m^2 & n^2 & 2mn\\ n^2 & m^2 & -2mn\\ -mn & mn & m^2-n^2\end{bmatrix}$$

where $m=\cos\theta$ , $n=\sin\theta$ as shown in Figure 29.

*Figure 29 Positive θ*

With this transformation the reduced transformed matrix is defined as:

$[\bar{Q}]=[T]^{-1}[Q][T]^{-T}$ , which relates the global stresses with the global strains.

$$\begin{bmatrix}\sigma_x\\ \sigma_y\\ \tau_{xy}\end{bmatrix}=[\bar{Q}]\begin{bmatrix}\varepsilon_x\\ \varepsilon_y\\ \gamma_{xy}\end{bmatrix}$$

The strains at any point of the laminate can be related to the strains at the reference plane ($\varepsilon^0$) and the laminate curvatures ($\kappa$). Figure 30 shows the coordinate notation on a laminate.

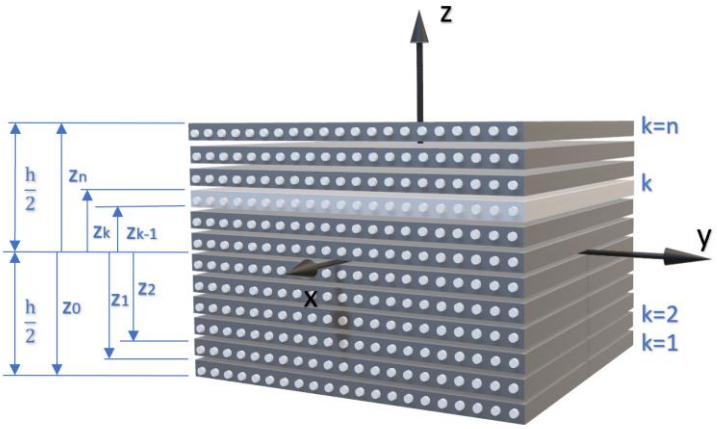


$$\begin{Bmatrix} \varepsilon_x \\ \varepsilon_y \\ \gamma_{xy} \end{Bmatrix} = \begin{Bmatrix} \varepsilon_x^0 \\ \varepsilon_y^0 \\ \gamma_{xy}^0 \end{Bmatrix} + z_k \begin{Bmatrix} \kappa_x \\ \kappa_y \\ \kappa_{xy} \end{Bmatrix}$$

*Figure 30 Laminate with coordinate notation of individual plies*

The laminate stiffness matrixes relate general load with the deformation of the laminates. Figure 31 shows the force and moment resultants from a load applied to a single lamina.

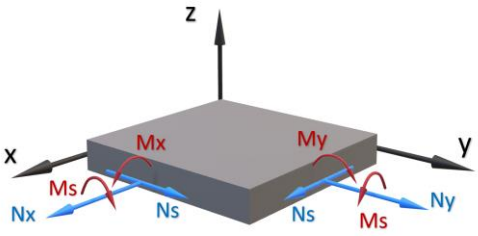


$$\begin{bmatrix} N_x \\ N_y \\ N_s \\ M_x \\ M_y \\ M_s \end{bmatrix} = \left[\begin{array}{ccc|ccc} A_{xx} & A_{xy} & A_{xs} & B_{xx} & B_{xy} & B_{xs} \\ A_{xy} & A_{yy} & A_{ys} & B_{xy} & B_{yy} & B_{ys} \\ A_{xs} & A_{ys} & A_{ss} & B_{xs} & B_{ys} & B_{ss} \\ \hline B_{xx} & B_{xy} & B_{xs} & D_{xx} & D_{xy} & D_{xs} \\ B_{xy} & B_{yy} & B_{ys} & D_{xy} & D_{yy} & D_{ys} \\ B_{xs} & B_{ys} & B_{ss} & D_{xs} & D_{ys} & D_{ss} \end{array}\right] \begin{bmatrix} \varepsilon_x^0 \\ \varepsilon_y^0 \\ \gamma_{xy}^0 \\ \kappa_x \\ \kappa_y \\ \kappa_{xy} \end{bmatrix}$$

*Figure 31 Force and moment resultants*

Where

$$A_{ij} = \sum_{k=1}^{n} Q_{ij}^k (z_k - z_{k-1})$$

$$B_{ij} = \frac{1}{2} \sum_{k=1}^{n} Q_{ij}^k (z_k^2 - z_{k-1}^2)$$

$$D_{ij} = \frac{1}{3}\sum_{k=1}^{n} Q_{ij}^{k}(z_k^3 - z_{k-1}^3)$$

For the special case of symmetric balanced laminates, engineering properties can be derived as a function of laminate stiffnesses with simple relations.

$$E_x = \frac{1}{h}\left[A_{xx} - \frac{A_{xy}^2}{A_{yy}}\right] \quad E_y = \frac{1}{h}\left[A_{yy} - \frac{A_{xy}^2}{A_{xx}}\right] \quad G_{xy} = \frac{A_{xx}}{h}$$

## References

Daniel, I.M. and O. Ishai, *Engineering Mechanics of Composite Materials*. 2nd ed. 2006: Oxford University Press.

# ANNEX II

## *SUSTAINABLE DEVELOPMENT GOALS*

In 2015 all the United Nations Member States adopted the 2030 Agenda for Sustainable Development. It includes 17 goals, which are related to the three dimensions of sustainability: economy, society, and environment. In the social dimensions the goals are: no poverty; zero hunger; good health and well-being; quality education; gender equality; affordable and clean energy; sustainable cities and communities; and peace, justice and strong institutions. The economical dimension includes the goals: decent work and economic growth; industry, innovation, and infrastructure; reduced inequalities; and responsible consumption and production. The environmental dimension advocates for life on land; life below water; clean water and sanitation; and climate action.

As with all the new technologies, the issue of sustainability in Additive Manufacturing has not arisen in early steps of its development in a consistent manner. The consequences of new technologies are always hard to predict. However, the impact of their use should be anticipated to adopt measures in order to work towards a more sustainable industry.

The impacts of Additive manufacturing have effects on the three sustainability dimensions. A schematic is shown in Figure A II 1.

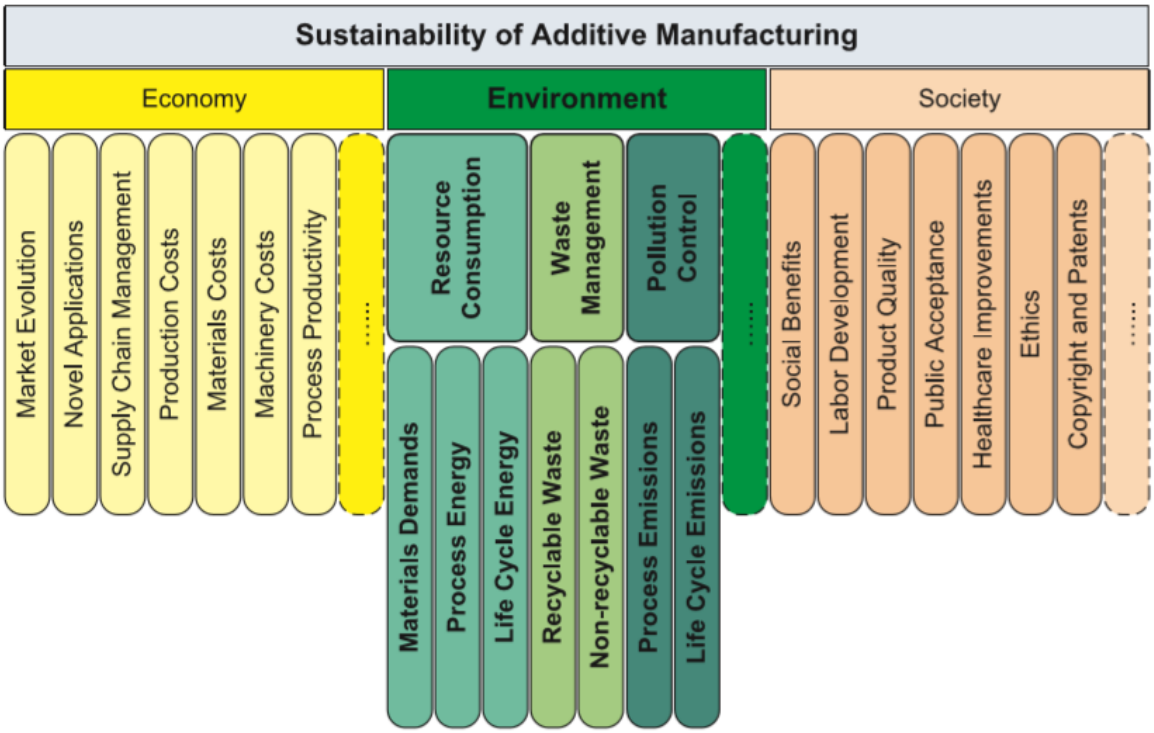


*Figure A II 1 Additive manufacturing sustainability impact [1]*

In the research conducted by Peng et al.[1] the environmental dimension was approached from three aspects: resource consumption, waste management and pollution control.

- Resource consumption: The main resources consumed by AM are materials and energy. Apart from the primary materials for the construction of the parts, secondary materials (support structures), protective gas and cooling water is needed for the production. Even though the material efficiency for AM processes can be as high as 97%, in practice this is never achieved. Energy is needed not only for the main AM equipment but also for auxiliary sub-systems. Long processes at elevated temperature require large amounts of energy and lead to low productivity rates.
- Waste management: Compared to subtractive manufacturing, the waste production in AM can be reduced by a maximum of 90%. Nevertheless, these technologies also produce unusable material. Efforts toward recyclability of

powders in powder bed fusion technologies, minimizing the material of support structures or reducing scrap material are yet to be done to ensure a more sustainable manufacturing.

- Pollution control: The need of toxic chemicals, like abrasive substances, forging lubricants or cutting liquids is avoided with 3d printing. In addition, less transportation is required due to decentralized manufacturing. However, AM processes still pollute in the form of gas, liquid, solid and sound. For instance, in FFF, ultra-fine particles emissions are reported, which increase the concentration of harmful particles in air if the working environment is not properly vented.

In spite of the limitations of AM, it can benefit the environment when compared to traditional methods. The demand of raw material in the supply chain is reduced; the processes require less energy, produce less waste, and pollute less; the design can be customized for the particular function of the part, improving its performance; the carbon footprint is improved since the materials transported are lighter and the production is decentralized.

Among the sustainable development goals, this project is aligned with the goal 12: Ensure sustainable consumption and production patterns. The target within this goal is the statement 12.5: “By 2030, substantially reduce waste generation through prevention, reduction, recycling and reuse” [2]

This project has contributed with computational simulations and instructions for the characterization of a failure surface for printed materials.

Computational simulations reduce the consumption of resources. The development of theoretical models to predict mechanical performance of the final parts is essential to find the optimal design. The shape can be adapted to a particular function so that lighter parts can be used without strength reduction. In addition, the number of tests performed before finding the right design is substantially reduced. Since many parameters are involved in the process of

printing parts, the number of possible combinations rapidly increases. With simulation software the best printing conditions can be found without the need of testing them all.

The characterization of a failure surface is needed for the computational analysis. Performing tests to determine the maximum strength of the materials in every failure mode provides information to future designers. This information is not only useful for simulation software but also is crucial to decide on the most suitable material for a particular application.

Although no experiments could be conducted in this project the information collected can be useful for future work.

## References

[1] Peng, T., et al., *Sustainability of additive manufacturing: An overview on its energy demand and environmental impact.* Additive Manufacturing, 2018. **21**: p. 694-704.

[2] *Sustainable development goals*. Available from: https://sustainabledevelopment.un.org/sdg12.